THESIS FOR THE DEGREE OF LICENTIATE OF ENGINEERING

Predicting moisture-related degradation risks across facades

Methodologies for moisture risk assessment across entire facades: Engineering and Data-Driven Approaches

JAN MANDINEC

Division of Building Technology

Department of Architecture and Civil Engineering

CHALMERS UNIVERSITY OF TECHNOLOGY

Gothenburg, Sweden 2025

Predicting moisture related degradation risks across facades
Methodologies for moisture risk assessment across entire facades: Engineering and Data-Driven Approaches
MANDINEC JAN

Technical report no 2025:3
Lic/Architecture and Civil Engineering / Chalmers University of Technology

Department of Architecture and Civil Engineering
Chalmers University of Technology
SE-412 96 Gothenburg
Sweden
Telephone + 46 (0)31-772 1000

Cover:
The satellite image of the case study neighborhood with the facades of interest highlighted.

Chalmers Reproservice
Gothenburg, Sweden 2025

Predicting moisture-related degradation risks across facades

Methodologies for moisture risk assessment across entire facades: Engineering and Data-Driven Approaches

JAN MANDINEC
Department of Architecture and Civil Engineering
Division of Building Technology, Building Physics
Chalmers University of Technology

Abstract

Predicting facade deterioration due to microclimate effects is crucial for sustainable building management. Traditional hygrothermal assessments often neglect these microclimate effects, leading to underestimated moisture risks, localized degradation and increased maintenance costs. To address these limitations, research advocates for the transition from a one-dimensional to a multi-dimensional approach, using Computational Fluid Dynamics (CFD) to capture microclimate effects, though this method is complex and computationally intensive.

In this work two methodologies were developed—Engineering and Data-driven approaches—to assess moisture-induced degradation risks across facades, section by section. The Engineering approach combines semi-empirical wind-driven rain methods with solar irradiation analysis to model hygrothermal loads and risks. The Data-driven approach uses image-based analysis, 3D model data and climate data to train a machine learning algorithm for predicting degradation ratios.

The framework for Degradation Analysis over Facades was introduced to validate these methodologies and to provide degradation data for the Data-driven approach. Using drones and computer vision, the framework was applied to 16 case study facades in Gothenburg, Sweden. The analysis of degradation data reveals that south-facing facades are more damaged, while degradation patterns vary.

The Engineering approach, applied to a single, yet representative, facade due to the laborious simulation process, revealed discrepancies between the modeled and observable degradation. A better incorporation of the roof overhang into the chosen WDR method (Straube and Burnett method) would increase the accuracy of the approach. The Data-driven approach, applied to all 16 facades, performed well in predicting degradation using the test dataset, achieving R-squared (R^2) value of 0.978, but deviated when predicting degradation on the validation facade (R^2=-1.152), which was initially excluded from the analysis. This was attributed to the distribution shift that arises due to limited training data and unknowns introduced from prior maintenance.

Despite these limitations, both methodologies offer promising alternatives to full-facade moisture risk assessment using CFD. Although tested on a case from Sweden, these methodologies are broadly applicable. Ultimately, the Data-driven approach could offer a computationally inexpensive way to assess facades in entire neighborhoods.

Key words:

Hygrothermal, Risk assessment, Microclimate, Degradation, Status assessment, Computer vision, Machine learning, Brick, Facade

Förutsägelse av risk för fuktrelaterad nedbrytning av fasader

Metoder för riskbedömning av fuktskador på hela fasader: Ingenjörs- och datadrivna tillvägagångssätt

JAN MANDINEC
Institutionen för arkitektur och samhällsbyggnadsteknik
Avdelningen för byggnadsteknologi, byggnadsfysik
Chalmers tekniska högskola

Sammanfattning

Att förutsäga nedbrytning av fasader på grund av variation i mikroklimat är avgörande för hållbar byggnadsförvaltning. Traditionella hygrotermiska beräkningar bortser ofta från dessa mikroklimateffekter vilket leder till underskattade fuktrisker, lokal materialnedbrytning och ökade underhållskostnader. För att åtgärda dessa begränsningar förespråkar forskningen en övergång från en endimensionell till en flerdimensionell metod. Beräkningsströmningsdynamik (CFD) är en komplex och beräkningsintensiv metod som kan användas för att fånga mikroklimateffekter.

I detta arbete har två metoder utvecklats—Ingenjörs- och datadrivna tillvägagångssätt—för att bedöma fuktrelaterade nedbrytningsrisker över fasader, sektion för sektion. Ingenjörsmetoden kombinerar semi-empiriska metoder för slagregn med analys av solstrålning för att modellera hygrotermiska belastningar och risker. Den datadrivna metoden använder bildbaserad analys, 3D-modelldata och klimatdata för att träna en maskininlärningsalgoritm för att förutsäga nedbrytningen.

Ett ramverk för analys av nedbrytning av fasadmaterial introduceras för att validera de båda metoderna och för att tillhandahålla nedbrytningsdata för det datadrivna tillvägagångssättet. Med hjälp av drönare och datorseende tillämpades ramverket på 16 fallstudiefasader i Göteborg. Analysen av nedbrytningsdata visar att fasader vända mot söder drabbas av fler skador och att nedbrytningsmönster varierar.

Ingenjörsmetoden tillämpades, på grund av den arbetskrävande simuleringsprocessen på en representativ fasad. Metoden visade avvikelser mellan den modellerade och observerade nedbrytningen. En bättre implementering av taköverhäng i metoden för slagregnsberäkning (Straube och Burnett-metoden) krävs för högre noggrannhet. Den datadrivna metoden presterade väl i att förutsäga nedbrytning när den testades på de 16 fallstudiefasaderna, testdatasetet, med ett R-kvadrat (R^2) värde på 0,978, men visade sämre resultat för nedbrytning av valideringsfasaden (R^2=-1,152) vilken initialt exkluderades från analysen. Detta beror på den distributionsförskjutning som uppstår på grund av begränsad träningsdata samt oklarheter gällande tidigare underhåll av fasaderna.

Trots dessa begränsningar erbjuder båda metoderna lovande alternativ till fullständig fuktriskbedömning av fasader med CFD. Även om de testades på ett fall i Sverige är dessa metoder generaliserbara. Det datadrivna tillvägagångssättet kan på sikt erbjuda ett beräkningsmässigt billigt sätt att bedöma fasader i hela områden.

Nyckelord: Hygrotermisk, Riskbedömning, Mikroklimat, Nedbrytning, Statusbedömning, Datorseende, Maskininlärning, Tegel, Fasad

Acknowledgment

I would like to express my sincere thanks to my supervisors, Pär Johansson and Angela Sasic Kalagasidis, for their continuous help, guidance, encouragement, and support, especially when I returned to work after sick leave. Our supervision meetings are always inspiring and beneficial.

Moreover, I'd like to thank all the former and current members of the Buildings Physics research area for their help and the enjoyable times we shared. My gratitude extends to all my colleagues and friends in our wonderful division. Special thanks go to everyone I have shared, or am sharing, an office with. You make this place fun and welcoming.

I would also like to thank my friends outside the workplace for their never-ending support and encouragement. Finally, but most importantly, I would like to thank my family. Thank you, Mom and Dad, and thank you, Blanka and Emil. You have made me a better person, and you are always in my heart!

Jan Mandinec

Gothenburg, April 2025

List of Publications

This thesis is based mainly on the work presented in the following publications

Paper I: J. Mandinec, A. Sasic Kalagasidis, and P. Johansson, "Predicting Facade Deterioration: A Machine Learning Approach Using Drone Imagery and Microclimate Data," preprint submitted to the Journal of *Automation in Construction*, Jan. 2025

Paper II: J. Mandinec, A. Sasic Kalagasidis, and P. Johansson, "Engineering approach to assessing the impact of microclimate on degradation risks distribution across facades," Manuscript in preparation

Additional Publications

Other publications that are related to the content of the thesis are listed below:

Paper III: J. Mandinec and P. Johansson, "Towards an automatized and objective assessment of data from visual inspections of building envelopes," *Acta Polytechnica CTU Proceedings,* vol. 38, pp. 57–64, Dec. 2022, doi: 10.14311/APP.2022.38.0057.

Paper IV: J. Mandinec and P. Johansson, "Status assessment of buildings using existing data and identifying gaps in data from performance indicators," *J. Phys.: Conf. Ser.*, vol. 2069, no. 1, p. 012026, Nov. 2021, doi: 10.1088/1742-6596/2069/1/012026.

Paper V: Mandinec, J., Johansson, P. (2023). Microclimate modelling and hygrothermal investigation of freeze-thaw degradation under future climate scenarios. *Journal of Physics: Conference Series*, 2654(1). ttp://dx.doi.org/10.1088/1742-6596/2654/1/012146

Table of Contents

Part I

PREFACE

The need for moisture risk assessment across entire facades.

1. Introduction

This section presents the background to the moisture risk assessment of facades, highlights the research gaps and proposes research objectives. The section then concludes with an outline of the research and its scope.

1.1 Background and aim

Building renovations are widely acknowledged as essential components of the decarbonization of the building sector. The European Commission estimates that more than 220 million building units were constructed before 2001. Current projections indicate that 85-95 % of the existing buildings will still be in use in 2050 [1]. Consequently, many of these buildings will require energy retrofits to meet efficiency standards. However, to ensure the long-term success of these retrofits, they must be accompanied by well-planned maintenance strategies whereof proper moisture safety measures constitute its important part that preserves building integrity and performance.

In general, a building that is improperly maintained or with built-in moisture safety issues loses its energy performance at an elevated pace. The exterior surface of a wall, commonly referred to as the facade, plays a key role in this process. When the facade material becomes wet, its thermal conductivity increases, which in turn intensifies the heat losses through the building envelope [2], [3]. Consequently, prolonged exposure of facades to adverse weather conditions and their insufficient drying may result in the occurrence of degradation patterns. Cracks, spalling, and other mechanical damages then accelerate the moisture ingress, which not only intensify the rate of degradation but also further exacerbate the loss of energy performance [4].

The precise effect of moisture-related damage on the energy performance of the building is difficult to quantify as it coincides with natural aging of materials. The insulation materials, for instance, could undergo 12-80% performance reductions across different thermal performance metrics, depending on the insulation type and the degradation interval [5]. In consequence, such a drop in performance can have a significant impact on the performance of the whole building. Another influential factor is the degradation of Heat, ventilation and air conditioning (HVAC) systems. This was accentuated in a case study conducted by Eleftheriadis and Hamdy [6], who compared the performance of a single-family house in two simulation scenarios, one of which included the discussed modes of performance degradation. Such a scenario overconsumed 18.4% and 47.1% of more primary energy over 20 years compared to the other case [6].

In consequence, maintaining components in good condition not only ensures energy efficiency but also translates into significant energy cost savings. According to the U.S. Department of Energy, a proactive maintenance strategy which plans and prioritize renovation actions in a timely manner, is associated with a 12-18% cost reduction compared to reactive approach [7]. For building facades with cladding systems, cost savings depend on factors such as material performance degradation, minimum acceptable quality, service life, and repair frequency. This was demonstrated by Flores-Colen [8], who analyzed preventive and predictive maintenance strategies for five common facade claddings in Portugal (cementitious rendering, elastomeric coating, emulsion coating, ceramic tiling, and natural stone) using data from a large-scale study. Except for emulsion coating, where proactive maintenance led to a 17% cost increase, other cladding systems showed cost reductions ranging from 0.5% to 20%. Despite the clear benefits with preventive and predictive maintenance strategies, approximately 70% of

renovation decisions in Sweden are made only after a component has exceeded its service life [9].

Irrespective of the maintenance strategy, all the cost-optimization efforts are futile if degradation occurs sooner than anticipated. This point is illustrated in Figure 1. Despite a major refurbishment of the facades of the tall residential building, which included the installation of costly scaffolding and replastering, it took just approximately 10 years for parts of the facade to delaminate. It is noteworthy that the damage is localized to this and similar south-facing facades, while facades facing other directions do not show such deterioration. Primarily, this is due to wind-driven rain (WDR), which is the main driving factor for weathering of buildings in Gothenburg.

Figure 1 Localized delamination of render on a high-rise building in Gothenburg, Sweden. The degradation occurred approximately 10 years after a major renovation of the building's facade.

A similar example is shown in Figure 2. There, a south facing brick facade, which was renovated in 2013, exhibits numerous bricks subjected to spalling and efflorescence. Again, facades of the building oriented in other directions exhibit either no or negligible degradation.

Figure 2 Localized spalling degradation on a brick facade of a residential building in Gothenburg. Sweden. The facade was renovated in 2013.

Such a fast reoccurrence of degradation inevitably results in the premature need for renovation, a need that may not be financially feasible in the near future and will only intensify as the rate of deterioration can only accelerate. Therefore, regardless of the maintenance strategy taken, the renovation measures must be accompanied by proper preventive measures.

In practice, the risk of moisture-induced deterioration is ensured by following technical standards. ByggaF in Sweden is an example of a qualitative moisture risk assessment tool, providing a framework and set of checklists to reduce moisture risks treating buildings from planning to operation stage [10]. Apart from qualitative methods like ByggaF, the risk of moisture-related degradation can be assessed quantitatively by combining hygrothermal modeling and empirically-derived performance indicators. These combine dose response functions with critical moisture saturation exceedance, allowing, for example, to assess the risk of contamination by mold growth [11] and freeze-thaw degradation. The latter was probably the main degradation mechanism for the occurrence of degradation in the aforementioned cases (Figure 1 and Figure 2), repeatedly freezing and thawing the excess moisture due to WDR. Therefore, despite the accessibility of both qualitative and quantitative methods for risk assessment, premature material degradation still occurs, pointing to the main limitations of moisture risk assessment.

Fundamentally, hygrothermal performance indicators cannot predict the occurrence or progression of degradation. One of the few attempts to bridge this gap was made by Portal et al. [12] who coupled a heat and moisture model with mechanical assessment of a historic panel painting to study how its lime wood supports responded to changing climate conditions. In most cases, however, hygrothermal performance indicators are used to estimate the risk of

degradation, and the freezing and thawing mode of deterioration is no exception. Theoretically, these indicators could serve as proxies for coupled models, providing a simpler means of estimating the onset and progression of degradation. Such indicators correlate the number of freeze-thaw cycles (doses) with the progression of damage. Numerous laboratory studies have shown that increased freeze-thaw cycles lead to greater deterioration severity. These studies, which adhere to technical standards, assess the impact of freeze-thaw cycles on the compressive strength and the micro/macrostructure of bricks [13], [14], [15] and mortar [16], [17].

However, applying dose-degradation correlations to real building envelopes is not straightforward. Laboratory test conditions are often too uniform compared to the varied exposures that real facades experience. For instance, technical standards for testing natural stone (EN 12371:2010), calcium silicate masonry (EN 772-18:2011), or clay masonry (SIS-CEN/TS 772-22:2008) require that specimens remain fully saturated before and during each warming period, with cold exposure set to a fixed duration. In contrast, real facades are subject to uneven rain events, solar and long-wave radiation, and shading effects from nearby objects, all of which influence surface temperature and moisture content.

Mensinga [18], [19] has criticized these laboratory-based freeze-thaw resistance tests, arguing that they exaggerate real-world conditions. He highlights two main issues: the often-omnidirectional nature of frost exposure and the insufficient control of specimen moisture saturation. The latter, he suggests, may explain why some bricks deemed less resistant in lab tests outperform in real-world conditions. Furthermore, it takes only a single freeze-thaw cycle for a brick to undergo irreversible volumetric changes, leading to damage. As a result, the number of cycles required for observable facade deterioration in the field remains unknown. This uncertainty extends to other indicators, such as the modified winter index [20] and the freeze-thaw damage risk index [21]. As a result, hygrothermal performance indicators are used only to compare different building envelope designs to minimize degradation risks as shown by [22].

Nevertheless, minimizing the risk of moisture degradation using hygrothermal performance indicators still doesn't ensure the prevention of localized facade degradation. A typical hygrothermal assessment assumes one set of boundary conditions for entire facade. Real facades, however, are exposed to a variety of weather conditions that stem from factors like overshadowing or sheltering from wind-driven rain (WDR). Such microclimate across a facade then causes the exceedance of critical moisture conditions across some parts of the facade, driving the occurrence of localized degradation. Figure 3 illustrates the effects of microclimate on a south-facing never renovated brick facade.

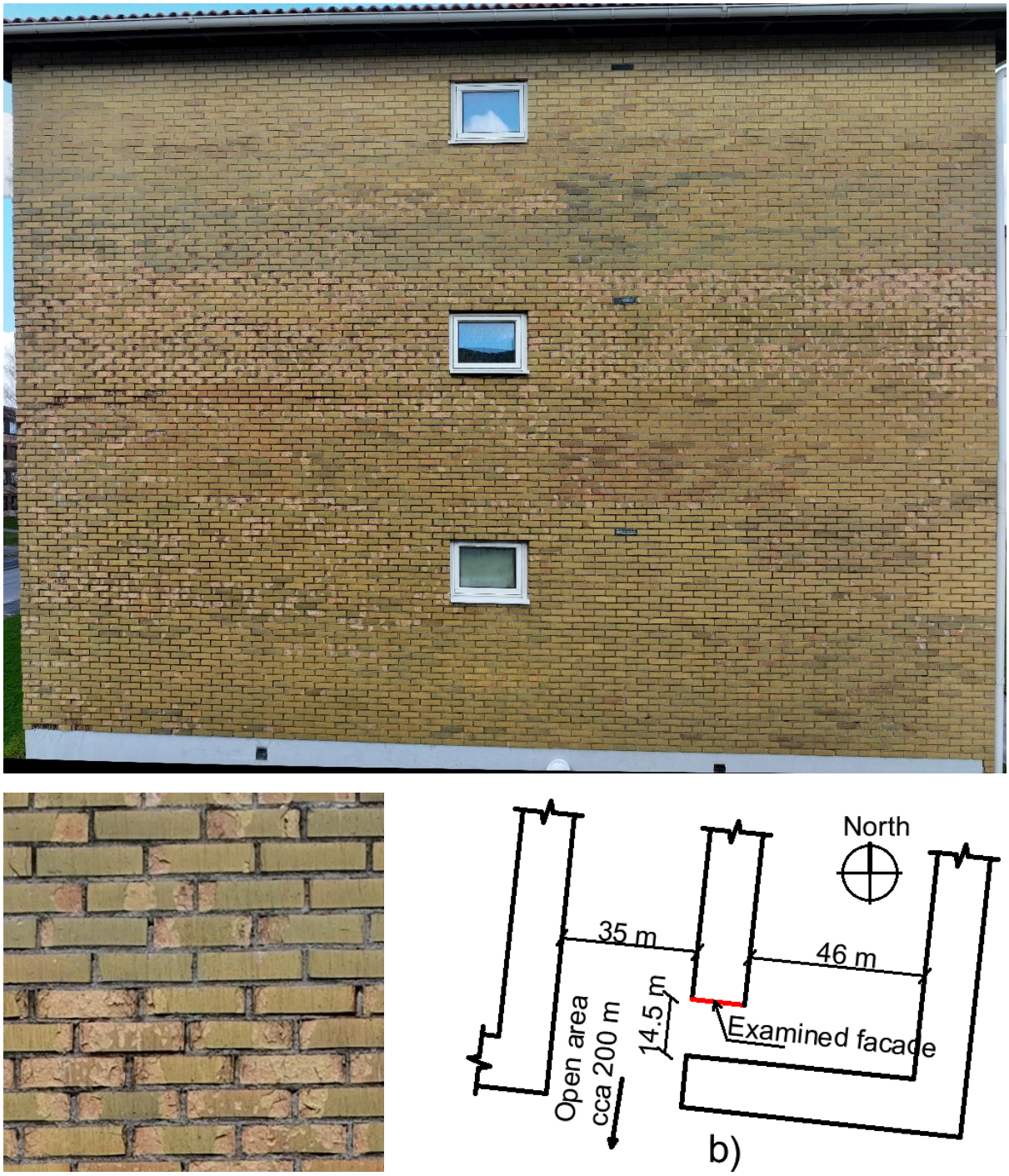

Figure 3 The effects of microclimate. Photograph on the top shows the brick part of a facade in Flatås, Gothenburg, Sweden. On the bottom left, there is a detailed view of the facade, showing bricks subjected to spalling. The drawing on the bottom right shows the facade situation with respect to the surrounding buildings.

The degradation primarily manifests as spalled bricks, forming a horizontal band across the central portion of the brickwork. Notably, the left side of the facade exhibits more pronounced deterioration, while areas beneath the roof overhang remain intact. A possible explanation for this pattern is the presence of a building in front of the facade. As illustrated in Figure 3, this building partially shelters the facade from wind and wind-driven rain, while leaving the left side exposed. Additionally, it provides shelter from solar radiation and sky radiation cooling.

Undoubtedly, studying the effects of microclimate can provide insights into the factors driving facade degradation, contributing to more effective conversion strategies. Recent research studies support this approach, advocating for the assessment of numerous points across a facade [23]. Despite this, hygrothermal assessments are still commonly conducted with a single set of boundary conditions for an entire facade. Therefore, the overarching aim of this thesis is stated as follows:

Overarching objective: Investigate methods for moisture risk assessment for entire facades.

In theory, a few microclimate modeling methods could be leveraged to produce unique boundary conditions across a facade. The area which was given the most attention in scientific literature is wind-driven rain (WDR). In practice, semi-empirical methods are employed. Those allow for the straightforward quantification of rain intensity impacting the facade surface. Typical examples of such methods are the technical standard (ISO 15927-3:2009) and the Straube and Burnett (SB) method [24]. Nevertheless, neither semi-empirical method is without limitations. Both methods, for instance, have been developed for use with a limited number of facade geometry configurations. Furthermore, the impact of surroundings is accounted for superficially at best. In this regard, the SB method does not consider this aspect at all, while a single number factor that is based on the surrounding's type is applied in the ISO standard to WDR. The limitations of the ISO standard have been partly addressed by Charisi and Thiis, who combined the standardized principles with ray tracing, which is a technique for modeling light transport. As a result, their methodology can account for the effect of small structural elements such as roof overhangs and window sill on the facade surface temperature and relative humidities [25], [26], [27].

Outside of the straightforward semi-empirical method and its derivatives, practitioners can make use of numerical simulations based on Computational Fluid Dynamics (CFD). Inherently, such an approach to WDR quantification is applicable to facades of complex geometries, while accounting for the urban environment. There has been significant progress in this area of research and several CFD models have been validated against field measurements for different building configurations [28], [29], [30], [31]. The validated models have been employed in further investigations within urban contexts [29], [32], also with the incorporation of radiation analysis [33]. Regardless of these advancements, from a pragmatic standpoint the use of CFD in practice is limited as it requires substantial computational power and is associated with long computational times. Moreover, CFD simulations require considerable domain expertise and are therefore complex in model setup and postprocessing.

The use of semi-empirical methods for WDR quantification, and following hygrothermal risk assessment, is preferable in practical applications. However, whether those methods can be combined with the short-wave and the long-wave radiation analysis to produce a distribution of degradation risks across facades that correspond with the observed degradation, is still an open research question. Thus, the first research objective is formulated as:

Research objective 1: Investigate the limitations of microclimate-based hygrothermal risk assessment from an engineering perspective.

Addressing the first research objective requires a methodology that follows the principles of hygrothermal modeling. This includes steps to define boundary conditions, perform coupled heat and moisture simulations, and interpret the results using performance indicators. However, a different approach can be proposed. In theory, empirical observations of moisture-induced

degradation and its spatial distribution across facades could be used for risk estimation / degradation prediction across other, yet undamaged facades. Providing such an estimator primarily requires an objective quantification of degradation across facades that could be achieved by analyzing Unmanned Aerial Vehicle (UAV or drone)-based imagery using computer vision. The conjunction of drone imagery and computer vision analysis is a growing field of research, aiming toward automation of anomalies detection. The greatest degree of attention in civil engineering has been devoted to crack detection. There, the research has moved from the generation of orthophotos with zoom-in functionality suitable for manual inspection [34], and traditional computer vision techniques such as Sobel edge detection and thresholding [35], [36], [37] towards deep learning algorithms. The latter has already been extensively applied to civil engineering structures [38]. However, the focus currently shifts on its application to facades, which inherently involves more background noise. For instance, Chen [39] developed a method for pixel-level crack segmentation, involving a two-step neural network that consists of Convolutional Neural Network (CNN) and U-net model. Nevertheless, the training of CNN, and especially the training of its convolutional layers, which extracts features from images, typically requires a substantial number of training images. Consequently, other researchers address this issue by employing the concept of transfer learning, whereby pretrained CNNs are leveraged for feature extraction, with the CNNs' classification layers then optimized for the detection of the desired degradation patterns. This concept has been used not only for crack detection [40], [41], but also for spalling and efflorescence [42], and spalling, peeling, biological growth and delamination [43].

Regardless of the detection method the obtained data is primarily used to assist in the building inspection process. The further use of such degradation data is limited to mapping it onto orthophotos [44] or 3D models [45] of buildings or analyzing crack characteristics [46]. The use of computer vision-based degradation detection and its spatial distribution across facades has not been employed to study microclimate in terms of geometric and weather exposure aspects of facades. This represents a missed opportunity to construct a machine learning predictor capable of estimating the impacts of microclimate in undamaged facades. Motivated by this, the second research objective is stated as follows:

Research objective 2: Explore the use of degradation data from UAV and computer vision to directly predict the impact of microclimate / degradation on facades.

1.2 Thesis outline

The central focus of this thesis is to present conceptual methodologies that address the research objectives and to demonstrate their practical applicability and accuracy in assessing/predicting moisture risk across facades. This is achieved by integrating a case study as a unifying narrative, within which the research objectives are systematically explored. The case study serves as a practical foundation, ensuring the methodologies' applicability and accuracy. The overall thesis structure, depicted in Figure 4, is organized into five parts:

- **Part I** establishes the rationale for moisture risk assessment across entire facades. It concludes by defining the case study, which involves 16 yellow brick facades.
- **Part II** introduces the theoretical foundation (methodology) for quantifying degradation across facades using UAVs and computer vision. It then applies these techniques to analyze the studied facades, generating degradation data that serves as input and target for evaluating the methodologies proposed in Part III.

- **Part III** presents methodologies (Engineering approach and Data-driven approach) for predicting risk of degradation across facades and demonstrates their application within the case study.
- **Part IV** presents the results, focusing on the comparison between predicted degradation risk and the actual degradation distribution observed through computer vision analysis.
- **Part V** discusses the applicability of the methodologies, offering conclusions and recommendations for future research.

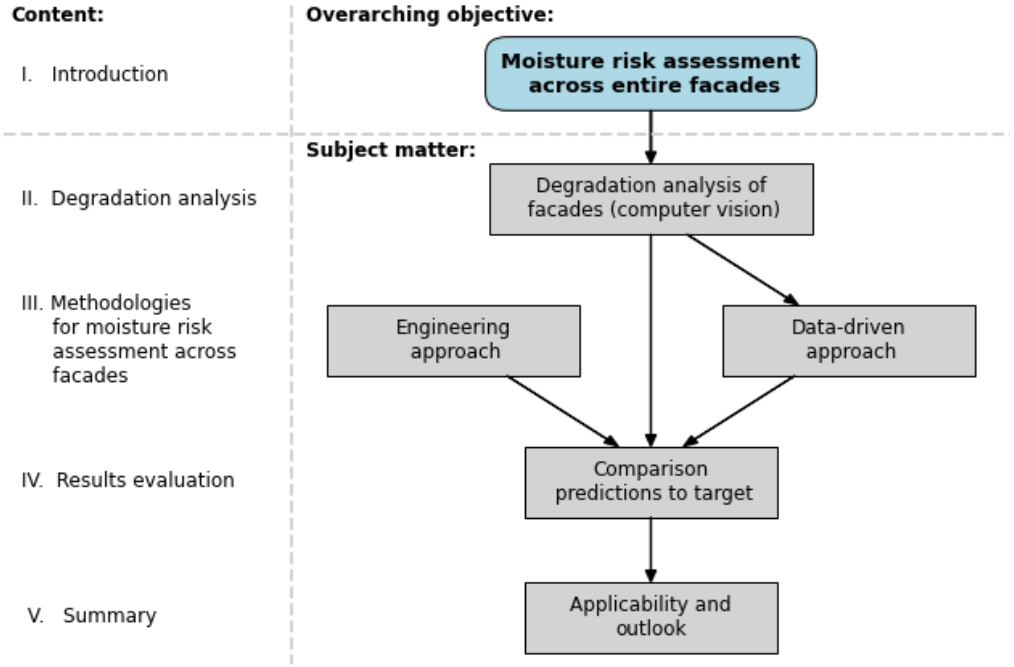

Figure 4 A flowchart showing the structure of this thesis

The content of Part II and segments of Parts III and IV, which are related to the Data-driven approach, is derived from Paper I. Paper II then forms the basis for the Engineering approach in Part III and its results in Part IV.

1.3 Scope of research

The case study, which permeates this thesis, comprises 16 facades located in a residential (Flatås) area in Gothenburg, Sweden, which were constructed between 1954 and 1965. Nine of the facades face south, two facades face north and east, respectively, and three facades face west.

Structurally, the facades can be divided into those with ventilated cavity and those without. Despite this distinction, all facades share a common outer layer consisting of yellow brickwork which covers lightweight concrete blocks. The brickwork is invariably underlain by a plastered lightweight concrete plinth. It should be noted, however, that the analysis and the subsequent predictions made by the methodologies focus exclusively on the area of brickwork. Table 1 summarizes the information about the facades studied. The location of the facades in the neighborhood is indicated in the title page figure of this thesis.

Table 1 List of facades used in the case study. Included is information regarding orientation, dimensions of the area examined (brickwork)

Facade index	*Address*	*Facade orientation*	*Dimension of brickwork [m]*	*Ventilated cavity?*
1	Svangrumsgatan 3	South	13.15 x 8.90	No
2	Svangrumsgatan 29	South	6.00 x 9.50	No
3	Armlangdsgatan 1	South	6.20 x 10.60	Yes
4	Synhallsgatan 16	South	6.32 x 8.00	Yes
5	Svangrumsgatan 53	South	5.00 x 9.00	No
6	Svangrumsgatan 36	South	6.00 x 11.40	Yes
7	Distansgatan 37	South	3.00 x 8.00	No
8	Synhallsgatan 17	South	4.00 x 13.98	No
9	Verktumsgatan 1	South	5.00 x 8.55	No
10	Armlangdsgatan 13	North	12.97 x 10.30	No
11	Synhallsgatan 22	North	6.26 x 9.50	Yes
12	Distansgatan 43	West	12.93 x 9.50	No
13	Svangrumsgatan 16	West	7.40 x 11.20	Yes
14	Svangrumsgatan 21	East	13.15 x 11.50	No
15	Svangrumsgatan 52	East	12.09 x 11.40	Yes
16	Synhallsgatan 5	East	4.00 x 13.40	No

All facades are subjected to a degradation analysis in Chapter II. Likewise, the Data-driven approach presented in Section 5 employs data from all the facades. On the contrary, the Engineering approach, presented in Section 4, due to its labor-intensive nature, is exemplified only on facade 1.

Part II

DEGRADATION ANALYSIS

“A goal properly set is halfway reached”

Zig Ziglar

2. Framework for degradation analysis over facades

This section presents a theoretical framework for systemic investigation facade degradation, enabling the detection, quantification, and analysis of its spatial distribution.

2.1 Framework overview and objective statement

The purpose of the framework is to organize the process of quantifying the extent of degradation and analyzing spatial characteristics across facades by structuring the workflow into three phases: Prepare, Train and Analyze, as illustrated in Figure 5. It guides data collection, algorithm training and result analysis.

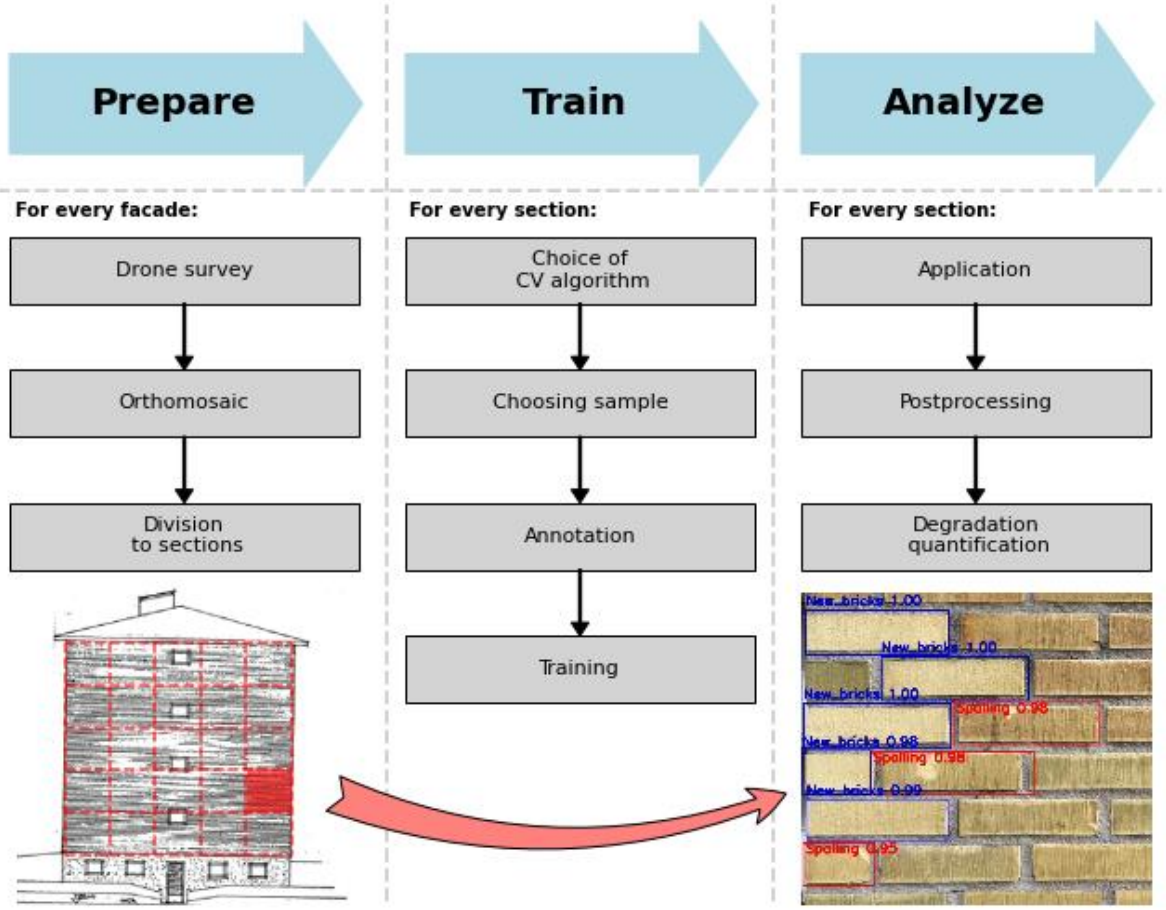

Figure 5 Framework for degradation analysis over facade. Each column represents a phase, i.e., Prepare, Train, Analyze, consisting of several steps.

The nomenclature of the phases is largely self-explanatory. In the Prepare phase, data are collected and prepared for the analysis, which is conducted in the Analyze phase. The latter phase, however, requires a computer vision algorithm that performs the analysis. The training of such an algorithm is handled in the intermediate Train phase but can be skipped if a pre-trained computer vision algorithm of a satisfactory performance is already available.

Before executing the framework, one must decide on the qualitative objective of the analysis and the desired performance metrics. The objective statement defines what degradation patterns, e.g., cracks, spalling, efflorescence, to look for. The performance metrics, on the other

hand, define how the degradations will be quantified. The most common metric for the assessment of facade is the area of degradation [47], but one can use other less common metrics or can invent a new one. For example, one may count the number of damaged bricks or estimate the severity of cracks by measuring their pixel width and orientation. Alternatively, one can measure the total (pixel) length of missing veneers etc. In the following, each phase is described in more detail.

2.2 Prepare

This initial phase involves the collection of photographs, their arrangement into orthomosaics and the subsequent division of orthomosaics into sections.

The collection of the photographs can be done by any means deemed appropriate since the framework does not impose any universal requirements, except that the deterioration of the facades must be recognizable. In practice, however, the rules for image collection (such as distance from a facade surface) must be established prior to the collection to ensure 1) consistency and, if a pre-trained computer vision algorithm is available, 2) compatibility of the images with what the algorithm has been trained to detect.

Based on experience, it is more appropriate to use Unmanned Aerial Vehicles (UAV's or drones) to collect images than to take photographs from the ground. This is due to their inherent quality for close-up and normal-direction shots. Nevertheless, ground photography can still be a sufficient option, especially for facades of smaller proportions. Beyond a certain spatial limit, however, which depends on many factors like the quality of a camera and lighting, a significant loss of detail is to be expected. Even so, this limit may be pushed further using various pre-processing techniques including sharpening, perspective transformation or deep learning upscaling [48]. Ultimately, the choice between drone and ground photography thus depends on the analysis target (i.e., spatiality of the facades) and its objectives.

Captured drone (or ground) imagery must be stitched together (or in the case of ground photography, its perspective transformed) to form an orthomosaic of a facade. This step can be achieved by any software for graphic editing including Adobe Photoshop or Affinity Photo. Alternatively, a specialized tools like Microsoft Image Composite Editor are available. The last step in the Prepare phase involves slicing on the orthomosaics to equally sized rectangular (or squarish) sections. The proportion of the sections is arbitrary.

2.3 Train

The choice of computer vision algorithms must be aligned with the objectives of the analysis and the performance metrics. A plethora of computer vision methods and approaches are available. The simplest is to use "classical" algorithms such as thresholding [49], k-mean segmentation [50] or Canny edge detection [51]. These, however, usually include hard-coded conditions to function that often make them sensitive and thus impractical when applied to larger numbers of images. The focus of the research has therefore shifted in the last decade to deep learning algorithms. Such advanced computer vision models, while requiring greater expertise, offer robust approaches to degradation analysis [52], [53]. These models can be categorized into 1) image classification, 2) object detection and 3) image segmentation. Their outputs differ and are illustrated in Figure.

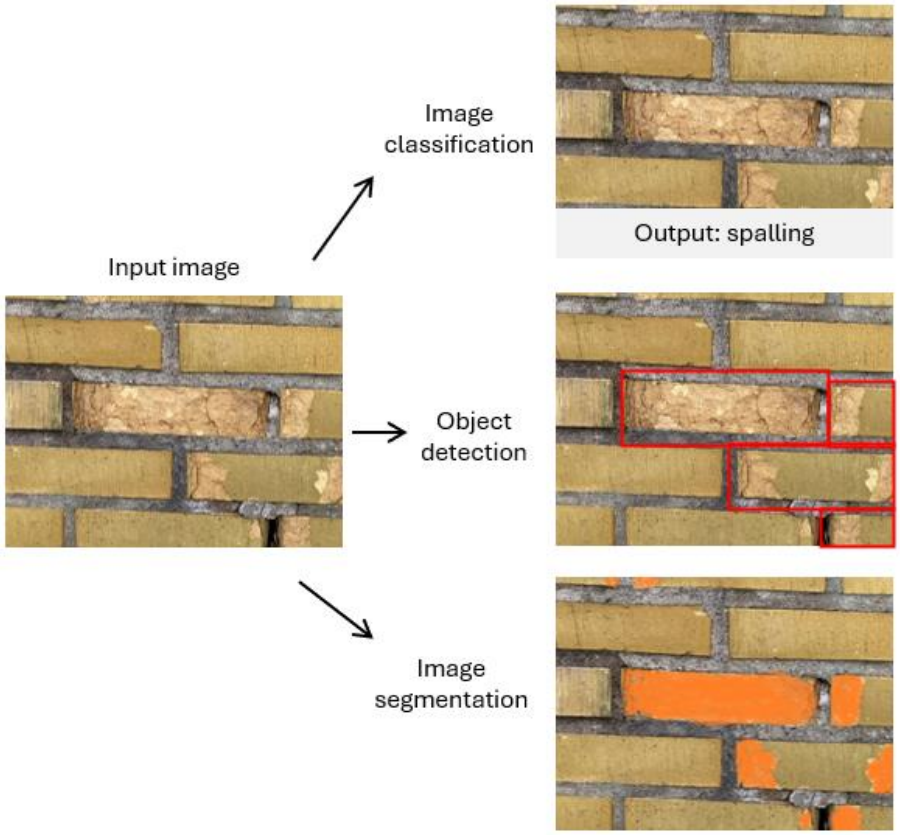

Figure 6 Comparison of outputs between image classification, object detection and image segmentation

Image classification algorithms, such as Inception [54] or ResNet50 [55] are ideal for binary degradation assessment, determining whether a section is affected or unaffected. Object detection algorithms, such YOLO (You Only Look Once) [56], EfficientDet [57], SSD (Single Shot MultiBox Detector) [58], are effective for detecting degraded bricks. Lastly, segmentation algorithms like U-net [59], FCN [60] or SegNet [61] are better suited for identifying cracks and missing veneers by coloring pixels associated with them. Although these algorithms are not natively designed for facade degradation detection, they can be retrained for this purpose. For instance, Wang et al. retrained Faster R-CNN [62] using 500 images to detect spalled and efflorescent bricks [63].

To retrain such algorithms, one needs images with the desired degradation patterns to train upon. A sample of the sections that were derived in the previously described Prepare phase is an optimal candidate for this purpose as it tunes the selected algorithm towards specificities observable on the studied facades. The optimal size of such a sample must be decided experimentally. Before the training process begins, each image in the sample must be manually annotated, either by providing a binary damaged or undamaged label in the case of image classification, or by highlighting the degraded areas in the case of object detection or image segmentation.

2.4 Analyze and the implications of framework's results

Once the training process is complete, the algorithm can be applied to each section of each facade, yielding raw degradation data across entire facades. These now need to be related to the chosen performance degradation metric to quantify the extent of degradation in each section. For instance, if a segmentation algorithm is used to highlight cracks, one can determine

the number of cracks in each section, classify whether a crack is horizontal, vertical or diagonal, or determine its width by counting pixels and relating them to the pixel size of objects of known dimensions.

The results from one section are comparable to those from other sections, enabling novel approaches to facade deterioration assessment based on quantitative evaluation rather than traditional qualitative methods. This shift has significant implications for analyzing and predicting facade deterioration. For instance, the results can support investigations into why some areas of facades deteriorate more severely than others, using empirical, image-based evidence. Furthermore, this transition from qualitative to quantitative assessment could facilitate the application of Markov chains for predicting degradation states. By leveraging quantitative degradation data across facades, it may even be possible to develop machine learning models capable of predicting deterioration on previously unobserved facades. The next chapter illustrates some of the new possibilities by performing the spatial degradation assessment of facades in the case study.

3. Degradation analysis - implementation

This chapter employes the proposed framework for degradation analysis of facades in the case study. The practical description of the framework implementation is complemented by the results from the degradation analysis.

3.1 Implementation

The objective of the case study is to quantify the spalling degradation across the brickwork of the facades using a variation of the area of degradation, i.e., the proportion of degraded bricks in a section, hereafter referred to as the degradation ratio, as a performance metric.

Upon investigating the facades, it was clear that bricks in some areas have been previously replaced as visible in Figure 7. These may be also considered as degraded to obtain a more comprehensive picture about where the degradation occurs. Therefore, before conducting the degradation analysis, a survey of building owners was undertaken to gather facade renovation histories. However, most efforts to pinpoint replaced brick locations and restoration dates were unsuccessful, with only the date of the most recent replacement identified. Thus, the analysis focuses on physically degraded bricks (e.g., spalling) and clearly replaced ones.

Figure 7 Example of the spalled and replaced bricks (bricks of noticeably brighter color) on a facade from the case study. Both are considered degraded for further analysis.

The execution of the framework was initiated by conducting a drone survey of the 16 facades using the DJI Mavic 3, equipped with a 4/3 CMOS Hasselblad camera. The operation of the drone was executed manually. Photographs were taken under overcast conditions, with the distance from the examined facade surface ranging from 3 to 6 meters, depending on the surrounding environment. The photographs for each facade were then stitched together into facade orthomosaics using Microsoft Image Composite Editor.

The objective for the subsequent sectioning of the orthomosaics was to obtain sections capturing approximately 1 m^2 of actual facade area. To ensure approximate agreement to this objective, it was essential to obtain reasonable proportions of the studied areas of the facades.

This was done by combining on-site measurements, including the measurement of the distance from the ground to the examined area and its width, with a three-dimensional model of the neighborhood, obtained from the Digital Twin Cities Centre (DTCC) model [64]. The areas of interest on the facades were modeled within the DTCC's model and divided into 1 m^2 sections using Rhino 7. These sections were then used to segment the orthomosaics accordingly, ensuring consistency between the physical measurements and the digital model. It must be noted that prior to the use of the DTCC's model, the height of the buildings was checked using technical documentation for one of the buildings.

To perform the degradation analysis, an in-house YOLOv4-based model capable of detecting spalled and efflorescent bricks as well as missing veneers in a stone masonry wall [65] was chosen for its capabilities and convenience. The model's performance, however, was deemed insufficient during the initial testing, likely due to its inadequate robustness. Therefore, the model was tuned to the specific appearance of the degradation and the other visual characteristics of the case study facades. This re-training was done by using a sample of 5 to 8 manually annotated sections from each facade, obtaining 90 images in total. These were divided based on the 80:20 rule to the training set and the test set. The re-training was conducted three times, with each model focusing on learning to detect different objects i.e., spalled bricks, replaced bricks and bricks.

The maximum number of iterations, referred to as "max batches," was set to 2000 for the algorithm. Training each model took approximately 10 minutes on an Intel(R) Core(TM) i9-10900 CPU @ 2.80GHz, equipped with an NVIDIA GeForce RTX 2070 SUPER GPU. The models achieved average precisions of 99% for brick detection, 87% for replaced brick detection, and 90% for spalled brick detection. An example of the models' output is shown in Figure 8, where the models detect spalled and replaced bricks.

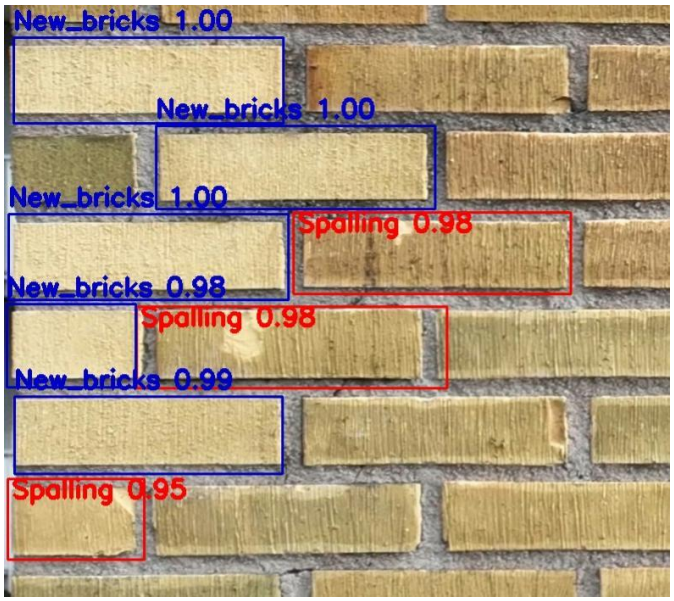

Figure 8 Output from the two models for detection of the replaced and spalled bricks.

The models were then applied to all facade sections, and the degradation area was calculated by counting the number of degraded bricks in an image divided by the number of bricks in an image (degradation ratio). The results were stored in a database for further analysis and visualization, which is presented in the following subsection.

3.2 Summary of degradation analysis

The results from the analysis are illustrated in Figure 9 which shows distribution of degradation ratios across all facades.

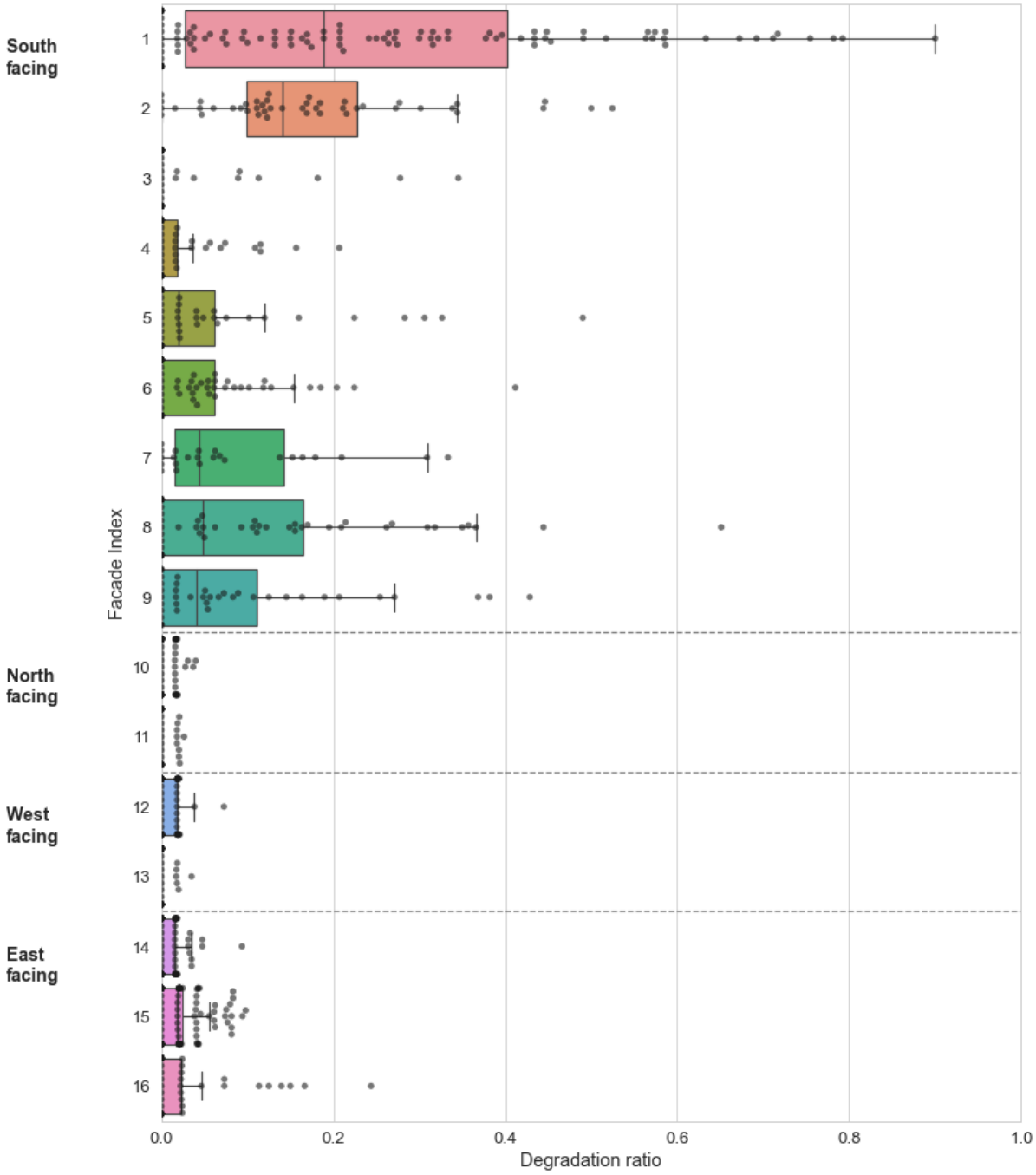

Figure 9 Degradation assessment of all facades using YOLOv4 model

The degradation distribution shown in Figure 9 are generally skewed towards zero. Of the 1171 facade sections analyzed, 672 (57.4%) were undamaged, and 909 (77.6%) had degradation ratios below 0.05. Such low degradation is most common in north, west, and east facades, where only 26 sections exceed this threshold. Even among outliers, the degradation ratios remain below 0.2, except for one section in facade 16, where 24.3% of bricks were classified as degraded or replaced. In contrast, south-facing facades show significantly higher degradation levels. While

the third quartile (Q3) degradation ratios for north, west, and east facades never exceed 0.025, south-facing facades exceed this value in seven instances, reaching 0.05 or more. Additionally, the upper whiskers of the box plots, representing 1.5 times the interquartile range (IQR), are consistently higher for south-facing facades, indicating more severe conditions. Figure 10 highlights the positioning and prevalence of degradation on the south-facing facades.

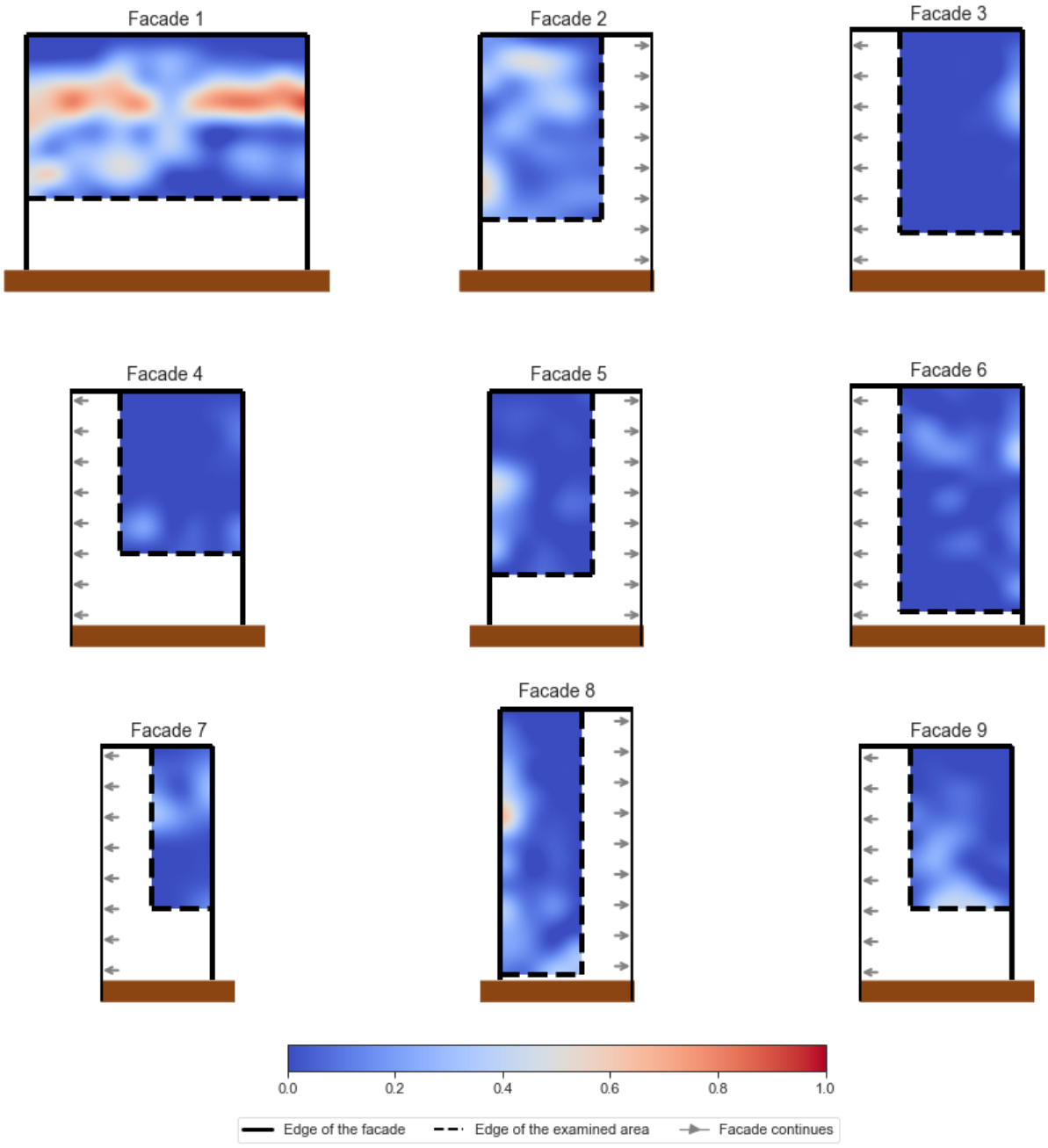

Figure 10 Spatial distribution of the degradation ratio on south-facing facades. Heatmaps were generated by upscaling degradation data arrays (sections) by a factor of 100 using spline interpolation. The facades are depicted to their actual scale.

Figure 10 illustrates that degradation is generally more pronounced along the edges of facades, marked by thick continuous lines, except for facade 9, where degradation is concentrated near the dashed line. Most facades also exhibit damage in their lowest portions. Notably, only facades 3, 6, and 8 have bottom edges within 0.5 meters of the ground, suggesting

potential capillary suction. However, facade 3's lower sections appear less affected compared to facades 6 and 8. For other facades, with lower edges positioned over two meters from the ground, rainwater runoff seems a more plausible cause of degradation. Below the brickwork, the lightweight concrete render facilitates water runoff.

Degradation patterns also appear around the middle or upper third of the facades. Facade 1 shows a prominent horizontal strip of damage just above the midpoint, with minimal degradation above it due to the roof overhang. In contrast, facade 2 has clusters of degradation above its midpoint, with the most prominent cluster closer to the upper edge, despite having the same roof overhang as facade 1.

Despite similarities in degradation patterns, each facade exhibits unique damage characteristics. For example, facades 2 and 5 are almost identical in design but differ significantly in their levels of deterioration. Similarly, other facades, such as facades 1 and 4, display distinct degradation patterns when compared to the rest.

The case study's degradation analysis offers unique insights into the prevalence and distribution of spalling across the facades. It highlights how facade microclimates influence surface conditions, leading to variations in the risk of physical degradation. This data serves as a foundation for developing methodologies to assess and predict degradation risks, providing a measurable target for validation, and in the case of machine learning models data to learn degradation patterns from.

PART III

METHODOLOGIES FOR RISK PREDICTION ACROSS ENTIRE FACADES

Development of methodologies to address challenges in the assessment of hygrothermal risks across entire facades

4. Engineering approach

The aim of this chapter is to address Research Objective 1: Investigate the limitations of microclimate-based hygrothermal risk assessment from an engineering perspective. This is done by proposing a methodology that uses readily available engineering tools and methods to assess the risk of moisture degradation across an entire facade. The chapter is divided into theoretical sections in which the methodology is described, and an implementation section in which the methodology is used to assess one of the facades in the case study.

4.1 Overview of the methodology

The proposed methodological framework for the assessment of the risk of moisture related degradation across facades consists of three steps. The first step is microclimate modeling, in which the scrutinized facade is segmented like in the degradation analysis (Section 2, to which hygrothermal boundary conditions are assigned, considering the facade's weather exposure and surroundings. Leveraging the boundary conditions in the next step, hygrothermal modeling is performed in each section. Its outputs are then processed in the final step of the methodology, assessing the risk of degradation by employing hygrothermal performance indicators. The overview of the methodology is summarized in Figure 11.

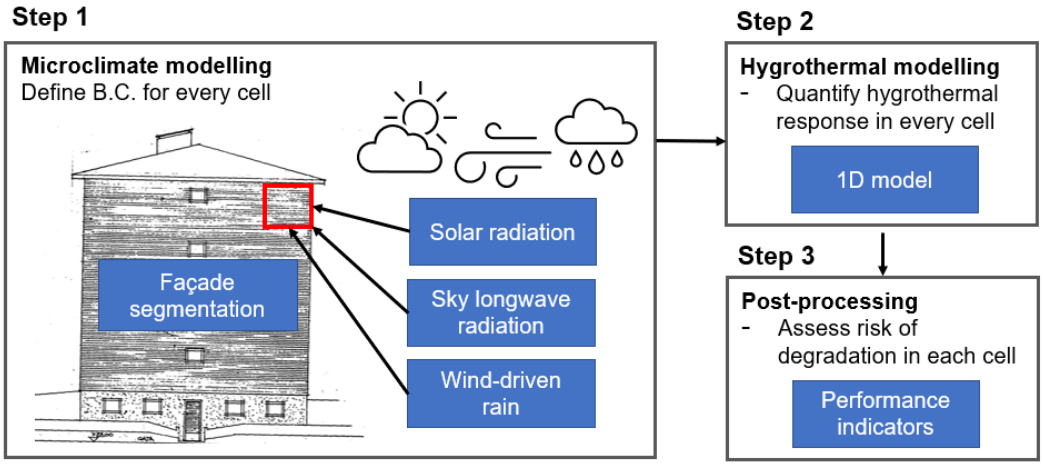

Figure 11 The engineering approach framework for assessing risks of moisture degradation across facades.

The methodology can be applied to assess the hygrothermal history of a facade and its sections, aiding in the study of how specific hygrothermal responses lead to degradation (as exemplified in Paper II). Alternatively, it can be used to predict degradation risks based on projected climate data (Paper III).

4.2 Microclimate modeling

Microclimate modeling focuses on defining boundary conditions for each facade section. This includes solar radiation, wind-driven rain and longwave sky-radiation cooling. The modeling is initiated by acquiring a three-dimensional model of a neighborhood that includes the facade under study with the roof overhang and the segmentation of the facade into sections. Furthermore, past or predicted hourly climate data is needed, depending on the aims of the study. Projected climate data is preferred to measured data because it eliminates potential missing data. The complete set of climate data required for modeling is given in Table 2.

Table 2 Required climate data for microclimate modeling

Variable	*Units*	*Purpose*
Direct normal radiation	W/m^2	Solar analysis
Diffuse horizontal radiation	W/m^2	Solar analysis
Atmospheric counter radiation	W/m^2	Longwave radiation
Horizontal rainfall intensity	mm	Wind-driven rain
Wind speed	m/s	Wind-driven rain
Wind direction	deg	Wind-driven rain

Several tools are available to convert climate data and building spatial characteristics into hourly solar irradiation, longwave radiation, and wind-driven rain data for each section of the analyzed facade. These include solar radiation analysis tools such as Ladybug [66], De Luminae [67], INDALUX [68] etc. However, none of these tools can fully handle all three aspects of the modeling.

Among these, solar analysis requires the least post-processing effort. For instance, Rhino 7 plug in Ladybug, which is utilized in the case study, can in one function segment facades and provide hourly irradiation data for the sections while accounting for surroundings and roof overhangs. However, this data does not include solar reflections from the surroundings, which can be incorporated during post-processing to enhance precision if needed. A detailed account of how to do this is presented in Paper II.

To perform the longwave radiation analysis, a balance equation is established. The incident longwave radiation exchange depends on contributions from atmospheric counter-radiation, the ground-reflected radiation, and terrestrial counter-radiation. These contributions are influenced by parameters such as the fraction of the sky visible to each section of the facade (sky-view factor, which can be determined in Rhino 7 or similar) and its complement, the terrestrial view factor. The ground-reflected radiation is determined by the long-wave reflectivity of the surroundings, while the terrestrial counter-radiation is based on the emissivity and temperature of the surrounding surfaces. The analysis assumes the surrounding surfaces behave as opaque grey bodies with temperatures equal to the air temperature. More details can be again found in Paper II.

Wind-driven rain (WDR) analysis requires the most extensive post-processing. Three semi-empirical methods are commonly used for WDR quantification: ISO 15927-3:2009, ASHRAE 160, and the Straube and Burnett (SB) method [24]. While all differ significantly, the ISO and ASHRAE methods are more advanced in incorporating influencing parameters, including correction factors for topography and surroundings.

The ISO method accounts for height-dependent wind speeds, typical roof overhangs, and six building geometry types. ASHRAE 160 uses a height-based correction factor but lacks provisions for roof overhangs, with wind applied uniformly. The SB method, though less comprehensive in parameters and limited to standalone configurations, distinguishes between high-rise and low-rise buildings, incorporates roof overhangs, and uses a power-law function for wind speed profiles.

All methods can map WDR distribution across a facade, assigning values to sections identified during radiation analysis. The SB method offers the most detailed mapping. Ultimately,

selecting the appropriate WDR method requires careful consideration of each method's strengths, limitations, and the objectives of the microclimate modeling.

4.2 Hygrothemal modeling

The methodology involves applying microclimate-based boundary conditions to hygrothermal simulations (coupled heat and moisture transfer), which can be performed using tools like WUFI 2D To maintain computational efficiency while analyzing numerous facade sections over extended periods, a 1D modeling approach is recommended. Key factors, such as explicit longwave radiation balance calculations and wind speed-dependent convective heat transfer, are incorporated to ensure accurate results. The indoor environment is typically modeled according to standards like EN 15026 to align with external climate conditions.

4.3 Post-processing

There are numerous hygrothermal performance indicators that can interpret the outcomes of the hygrothermal modeling, estimating the risk of moisture-related degradation. Among the most common is the exceedance of moisture content, estimation of condensation risks, assessment of drying potential or a mold growth index [11].

The risk of physical degradation due to weathering, for which this methodology is primarily, but not exclusively, designed, is frequently associated with freezing and thawing. Such a degradation is frequently assessed through moist freeze thaw cycles, which counts the number of times the material experiences a temperature drop below 0 °C while exceeding a certain relative humidity level. More advanced indicators, such as the modified winter [20] or the freeze-thaw damage risk (FTDR) index [21] also consider material properties and the severity of temperature drops. The FTDR index is particularly comprehensive, incorporating porosity and bimodal functions to estimate critical freezing temperatures and ice content.

As with microclimate modeling, the choice of the hygrothermal performance indicator requires careful consideration to align with the objectives of the modeling. Regardless of the chosen indicator, hygrothermal performance should be assessed across all facade sections, mapping variations in degradation risk.

4.4 Case study implementation

The methodology is exemplified on facade 1 (Figure 12a), which was in Section 3 and Figure 9, highlighted as the most profoundly damaged. The objective is to quantify the variation in freeze-thaw degradation risk across the brickwork of the facade and to compare it with actual degradation.

The investigated façade measures 13.5 x 11.5 m (Figure 12c), with the brick section starting 3 m above the ground. Validated climate scenario (A1B) projecting hourly weather data for Gothenburg, Sweden, from 1991 to 2021 is used to define the hygrothermal response of the façade. The considered dimensions of the facade and its brickwork part correspond to DTCC model [64], which were verified using technical documentation and on-site measurements where possible. The facade faces south and is sheltered by neighboring buildings (Figure 12b). One building, located 14.5 m in front of the facade, provides shelter from the south and east, while a second building, 35 m further to the west, also offers some shelter. An open area is present to the southwest.

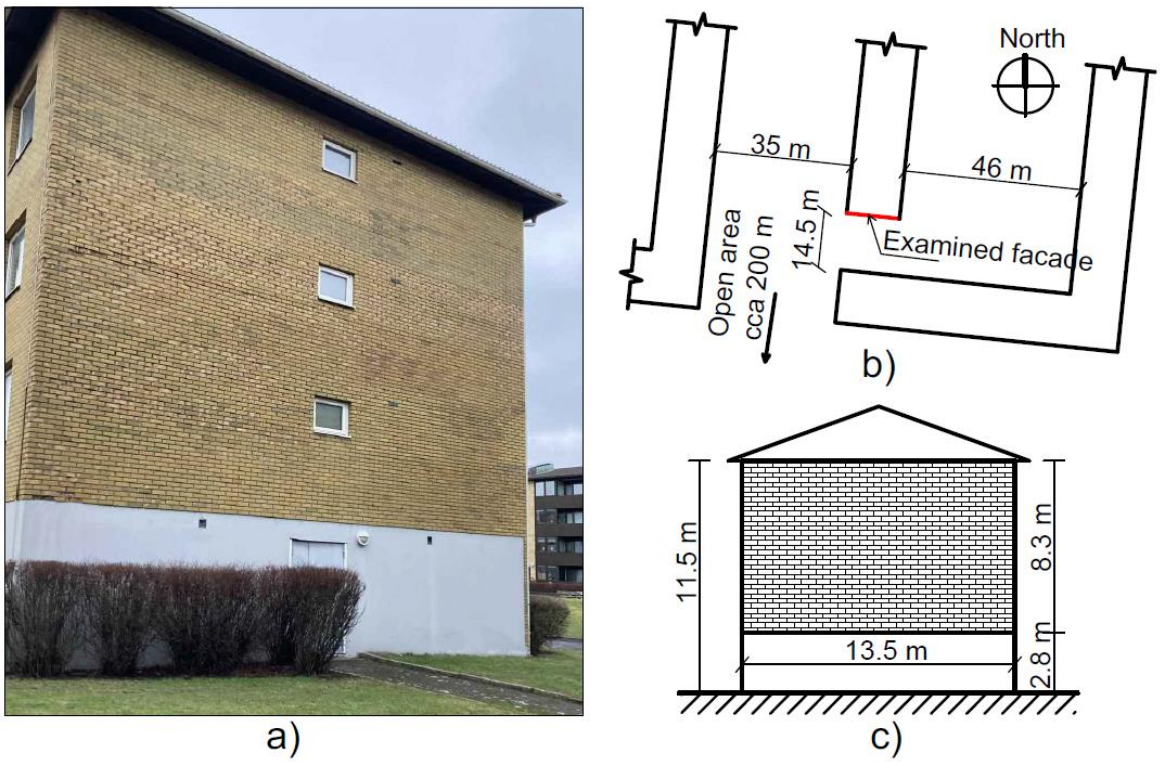

Figure 12 a) Photo of the case-study facade, b) footprints of the examined and surrounding buildings including dimensions, c) dimensions of the examined facade.

The brickwork of the facade was segmented into 104 sections, which corresponds with the sectioning performed in "3. Degradation analysis - implementation". Solar analysis and the acquisition of the sky-view factor for all sections were performed using Rhino 7. These were then transferred to the incident solar and longwave radiation using coefficients from Table 3.

Table 3 Coefficients for microclimate radiation modelling. All values are taken from the WUFI database [69].

	Value
Short-wave reflectivity of surrounding	0.2
Long-wave Reflectivity of surrounding	0.1
Long-wave Emissivity of surrounding	0.9

To quantify WDR over the sections, the SB method is chosen over the standardized ISO method regardless of its lack of parameters that can scale rain intensities based on neighboring buildings and terrain category (urban, suburban etc.). The SB method is preferred due to its ability to finely distinguish the effects of rain over a facade. It achieves this by providing maps of Rain Admittance Factor (RAF), a variable that scales the incoming rain over the facade surface. These maps are provided for several facade configurations. For the analysis, a configuration corresponding to a tall building is chosen due to the height of the facade being over 10 m. Figure 13 shows how the mapping prescribed by the method is applied to the facade under scrutiny.

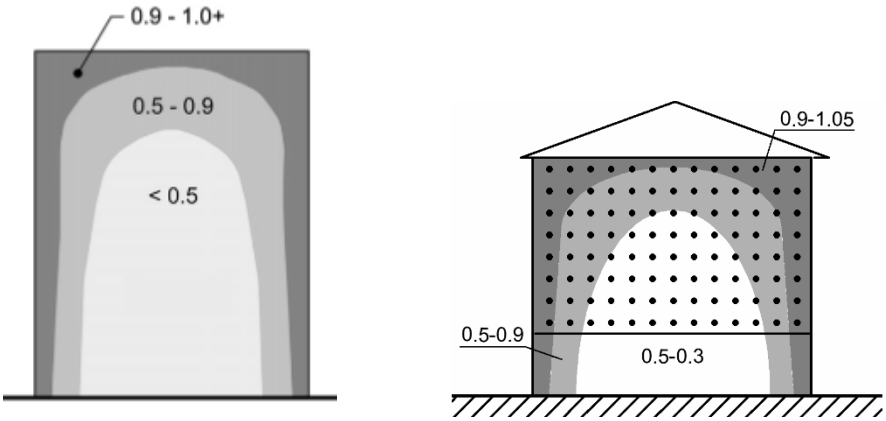

Figure 13 Mapping of the SB method to the facade under study. On the left is the prescribed RAF mapping for tall buildings with no roof overhang (>10m; H/W >> 1[45]). On the right is the adaptation of the mapping to the facade in question. The points on the right represent the centers of the individual sections. The resulting RAF coefficients are calculated based on interpolation within the range that can occur in each section. The extremes of each range are assigned to the edges of each area, with the inner area having its lower end located in the middle.

WUFI was chosen as the tool to perform hygrothermal modeling due to its convenience and its inherent ability to account for latent heat effects throughout the material. This quality is crucial for the accurate modeling of freeze-thaw behavior as phase changes of moisture—such as condensation and evaporation—release or absorb latent heat, affecting the temperature distribution.

The facade, which consists of hollow bricks (108 mm) and aerated concrete (200 mm) was modeled according to the technical documentation of the building. No material properties were found within the documentation thus WUFI material database was utilized, selecting *'Aerated clay brick (672 kg/m^3)*' and '*Aerated concrete (600 kg/m^3)*' are selected. Figure 14 shows a cross section of the facade and its discretization in WUFI into 58 and 92 computational cells.

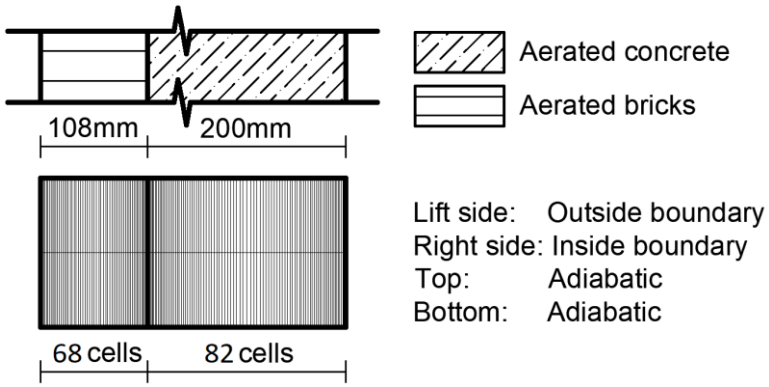

Figure 14 The two materials in the facade and their discretization into computational elements in WUFI 2D-3

To account for the specific microclimate at each of the 104 computational cells on the facade, a unique set of boundary conditions was defined for each cell, resulting in 104 individual models in WUFI. The initial temperature and relative humidity of the materials were set to the January 1991 averages: 1.75°C and 89% RH. The simulation time was set from January 1991 to the end of 2022.

The freeze-thaw damage risk (FTDR) index [21] was selected as the performance indicator for this case study. The risk is assessed at a depth of 2 mm below the surface to account for the material's inertia, which would otherwise lead to an overestimation if surface conditions were

used. The evaluation spans all 31 years of the climate sequence. Parameters from [70], also adopted by Zhou, are utilized for the assessment due to the unavailability of specific material data, as outlined in Table 4. However, the capillary moisture content parameter (w_{cap}) is adjusted to the specific value provided in the WUFI database.

Table 4 Parameters used for the calculation of the FTDR index.

	Aerated clay brick (672 kg/m3)	*Reference*
w_{cap}	291.0	[69]
l_1, l_2	0.18, 0.82	[70]
a_1, a_2	3.2e-8, 9.5e-7	[70]
n_1, n_2	3, 2.2	[70]

The results from the application of the engineering methodology are further presented in Section 6. Discussion of its limitations and applicability is provided in Section *7*.

5. Data-driven approach

The methodology proposed in this chapter aims to address Research Objective 2: Explore the use of degradation data from UAV and computer vision to directly predict the impact of microclimate / degradation on facades. Unlike its engineering counterpart, which uses conventional hygrothermal risk assessment methods, this methodology uses data and machine learning to assess moisture risks / predict degradation across entire facades. This chapter is again divided into a theoretical and an implementation section.

5.1 Overview of the methodology

The proposed data-driven methodology centers on constructing a machine learning algorithm (ML) to predict degradation across facades. This algorithm leverages image-based empirical evidence analyzed using the framework outlined in Section *2*. It also incorporates climate data and spatial information from a three-dimensional model of the facade neighborhood. The methodology consists of three steps, as shown in Figure 3.

The first step involves applying the *Framework for Degradation Analysis Over Facades* to generate target data for training the ML algorithm. The second step, referred to as "Integration," combines degradation data for each facade section with related features that influence degradation. This step emphasizes acquiring and aligning relevant data. Finally, the third step curates the integrated dataset and focuses on selecting, training, and testing the ML predictor.

5.1.1 Integration

After applying the *Framework for Degradation Analysis Over Facades* all facade orthomosaics should be segmented into sections, analyzed, and the resulting degradation data for each section stored in a database as the target variable. At this stage, the target variable must be supplemented with data features that include relevant environmental and spatial characteristics of the sections.

To achieve this integration, each facade under scrutiny in the 3D neighborhood model must first be segmented into sections corresponding to those used in the degradation analysis. Two types of features can be acquired by combining the 3D model and climate data: general, elementary and azimuth-based features. In addition to those, general information about the facades, such as the year of construction, year of renovation, and facade composition, can be collected. The elementary features include spatial factors that capture the influence of various modes of weathering. To capture the effects of WDR, these may include the height between the center of each section and the ground, or the horizontal distance of each center to the nearest corner of the facade. Moreover, to capture the longwave sky radiation, the sky-view factor should be collected.

Azimuth-based features integrate spatial characteristics with climate data to account for the effects of wind and wind-driven rain (WDR), while also considering surrounding buildings. This process involves breaking down weather factors like WDR into 36 directional components, each separated by 10° azimuths. The incoming rain is then scaled linearly based on the distance to the nearest object in each respective direction, considering objects at a distance 100 meters or longer without the obstructive effect. This process is illustrated in Figure 15.

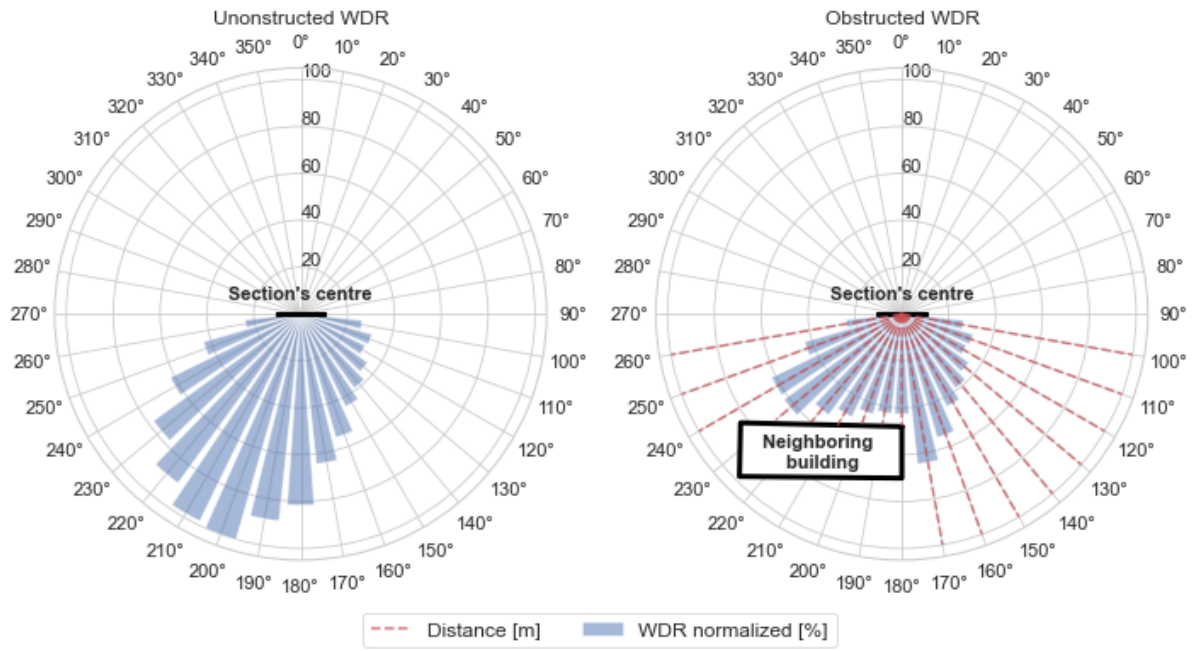

Figure 15 Accounting for obstruction from nearby objects in azimuth-based features. On the left, unobstructed wind-driven rain impinges on the center of a facade section. On the right, obstructed wind-driven rain is shown. The obstructions are considered by measuring distances in every azimuth visible from the section center, set apart 10° (red dashed line), and interpolated against the maximum of 100 meters.

It is important to note that the suggested features are not fixed within the methodology. Alternative features may be defined and could prove more impactful depending on the specific ML algorithm used. Experimentation with features is encouraged to optimize the model's performance.

Regardless of the features employed, the integration process may generate numerous features, leading to a large feature space and the risk of the curse of dimensionality, a concept introduced by Richard Bellman [71]. As dimensions increase, the feature space expands exponentially, requiring significantly more data to maintain adequate coverage. Consequently, data points may become sparse, obscuring underlying patterns. To address this, reducing the feature space is recommended before proceeding further.

Two common dimensionality reduction techniques to consider are Principal Component Analysis (PCA) [72] and binning. PCA transforms data into a new coordinate system aligned with the greatest variation, making it applicable to part or all of the database regardless of feature type. Binning, in contrast, aggregates similar features into groups, such as combining azimuth-based wind-driven rain (WDR) data from multiple directions.

5.1.2 Constructing a machine learning predictor

After the database includes the target variable and the explanatory features, the next step is to train an ML algorithm(s) for predicting degradation.

To construct such an algorithm, the relevant features must first be selected from the feature space. This step is critical for mitigating overfitting, reducing computational costs and enhancing the predictive performance of ML models [73]. The importance of a feature depends on several factors, including the strength of correlations, the linearity of underlying patterns, and the type of algorithm used (e.g., classification or regression) and its specific purpose. Consequently, feature selection often involves experimentation and multiple iterations.

The choice of a feature selection method depends on aspects such as the dimensionality of data and the available computational resources. Commonly used methods include filter, wrapper, and embedded approaches, with the latter often integrated within ensemble algorithms like random forests.

Selecting the appropriate ML algorithm itself depends on the nature of the data and the problem being addressed. For this methodology, algorithms capable of handling high-dimensional, potentially sparse data are preferred, such as decision trees, support vector machines, or ensemble methods like random forests. To ensure that the selected features generalize effectively to unseen data, strategies like hyperparameter tuning and cross-fold validation can be employed. These techniques help mitigate overfitting, a common issue where the model captures noise rather than underlying patterns in the data.

5.2 Case study implementation

The methodology is implemented onto the 16 facades of the case study, with the objective of training the ML algorithm for predicting degradation across facades.

5.2.1 Dataset generation

To acquire data for the algorithm, first the target variable, i.e., the degradation ratio of each facade section, is taken from Section 3. These are complemented with features generated in the Integration process, using the same DTCC neighborhood model as before. Three elementary features for the center of each section are derived, namely height from the ground, sky-view factor and distance from the closest edge of the facade. These are complemented by one categorical feature (Facade constant) which serves to distinguish between non-ventilated and three types of ventilated facades as defined in Table 1.

Azimuth-based features are generated for WDR while considering obstructions from neighboring objects. For this process, hourly weather data for Gothenburg, Sweden and the period between 1960 and 2023 are instituted. Data are derived from the validated climate scenario A1B and cover the exposure of the facades for most of their service life. Figure 16 illustrates the used wind and rainfall intensity data by presenting a wind-rose diagram and total rainfall by wind-direction.

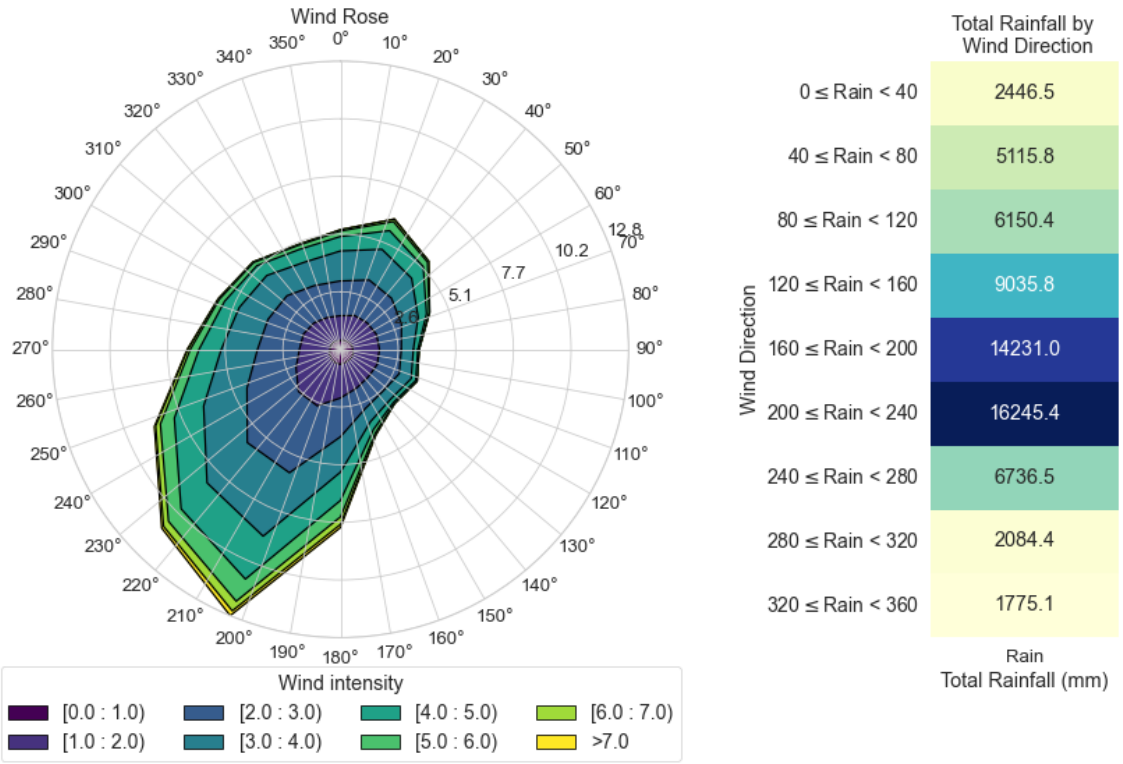

Figure 16 Wind and rain data for Gothenburg, Sweden, derived from the A1B climate projection for the period 1960–2023. The left panel presents a wind-rose diagram, illustrating the frequency and intensity of wind directions. The right panel displays a heatmap, summarizing the cumulative horizontal rain intensity, binned into 40° azimuth intervals, highlighting the directional distribution of rainfall over the study period.

The exposure intensity is notably higher on the south and southwest sides of the facades. The prevailing wind direction ranges between 200° and 210° azimuth, while the heaviest rainfall intensity is observed between 200° and 240° azimuth. The calculation of WDR-based azimuth features for each facade section utilizes rainfall intensity data during the winter months. The cosine rule, a foundational principle in widely used semi-empirical WDR methods, is employed to project precipitation onto the facade surfaces. These projections are further categorized into 36 directions, each separated by 10° azimuth intervals, and multiplied by the mean wind speeds for the corresponding directions, while accounting for neighboring obstructions as described in Section 5.1.1.

To reduce the dimensionality of the azimuth-based feature, binning, which aggregates WDR into bins separated by 40° azimuth intervals, and principal component analysis (PCA), which condenses the 36 dimensions into 2 principal components are used. These are complemented by the mean and sum of WDR values to finalize feature space. Altogether, the feature space comprises 17 features for constructing the machine learning predictor of degradation. Figure 17 presents the Spearman's correlations for these 17 features, displayed for individual facades, facades grouped by orientation, and the entire dataset.

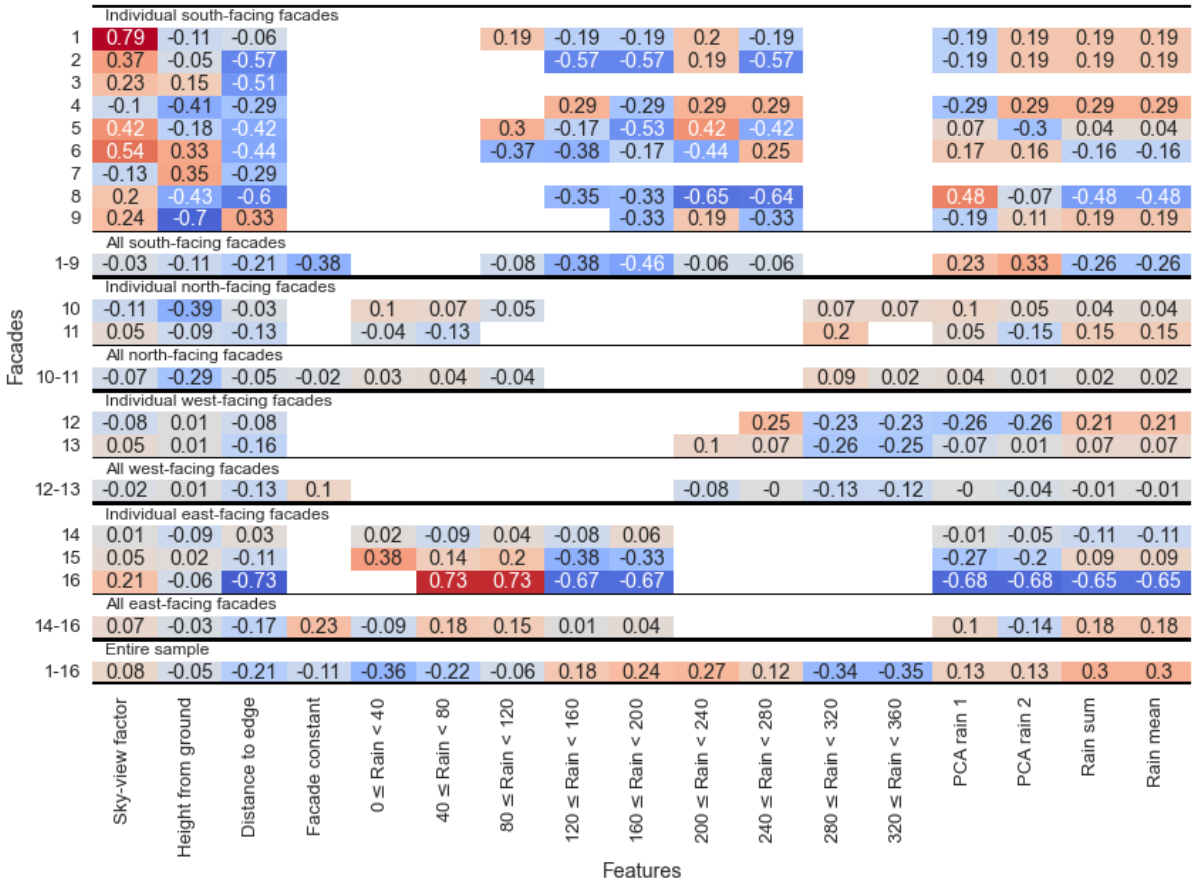

Figure 17 Spearman correlation coefficients of features with the degradation ratio across facades. In instances where data gaps existed, the correlation coefficient could not be defined due to the presence of constant input values, which prevented meaningful statistical analysis.

The features' correlations with the degradation ratio (the target) vary considerably across different facades. This can be illustrated on the south-facing facades, where the sky-view factor shows strong positive correlations to the target variable in some facades (e.g., facade 1; r=0.79) while displaying negligible and negative correlations at the others (facade 7; r=-0.13).

Grouping the facades to their respective orientation lessens the features' correlations, while preserving notable variability. The highest recorded positive correlation is weak and is associated by the second principal component in south facing facades (PCA rain 2 south-facing; r=0.33). Similarly, as before, the direction of the correlation for the features is flipped, exhibiting a weak negative correlation for east facing facades (PCA rain 2 east-facing; r=-0.14). Considering the entire dataset, weak or negligible correlations can be observed across the features.

5.2.2 Dataset apportion for performance testing and augmentation

Given the disparities between facades' distribution of degradation, as highlighted in Section 3.2, the performance of an ML predictor is to be evaluated assessing two aspects of generalization. The first aspect aims to assess the model's generalization ability to unseen data, which are drawn from the same degradation distribution as the training data. The second aspect aims to test the model against unseen data, which may be drawn from a different distribution than the training data. To achieve this, data for one entire facade is excluded from the dataset and thus from the training process, forming the hold-out (the validation) sample for. The remaining data are

augmented, shuffled and divided according to 80:20 rule into the training sample, and the second hold-out (the test) sample.

In practical terms, facade 2 is selected as the validation facade. The reason lies in the degradation analysis as presented in Figure 8 and Figure 9. Facade 2 is the second most degraded facade in the dataset after Facade 1. Unlike Facade 1, which shows significantly higher levels of degradation compared to the other facades and may be considered an outlier with degradation levels not representative of the rest, the high degradation ratios in Facade 2 could potentially be predicted based on data from Facade 1. Figure 18 shows a photograph of Facade 2 and a detailed view on the facade.

Figure 18 Photograph of Facade 2 (the validation facade). On the right is a detailed view of the area marked with a red mask in the photograph, illustrating replaced bricks and bricks undergoing spalling.

The validation facade encompasses data for 45 sections. The remaining data are augmented by a factor of 10, adding random Gaussian noise to the target variable. The resulting training and the test hold-out samples contain 9008 and 2252 datapoints, respectively.

5.2.3 Selection and tuning of ML algorithm

To construct the degradation predictor, a random forest regression algorithm was selected for its robustness against collinearity and overfitting, its ability to model complex relationships, and its inherent capability to assess feature importance. The model is constructed and its performance evaluated in two experimental set-ups, each incorporating both hold-up samples. In the first setup (Set-up 1), the random forest algorithm automatically selected features based on their importance, keeping those with an importance score exceeding the mean importance of all features. In the second setup (Set-up 2), the automatically selected features were augmented with manually chosen ones. This approach aims to assess the impact of varying feature

selections on the predictions for the validation facade, which, as previously noted, exhibits distinct degradation patterns compared to the rest.

To mitigate the risk of overfitting, hyperparameter tuning was performed using a grid search approach, systematically exploring a range of hyperparameter combinations to optimize model performance. The hyperparameter tuning process focuses on five key hyperparameters, deemed critical for constructing the random forest regressor.

1. **Number of Trees**: This parameter determines the total number of trees in the forest. The default value is 100 trees, but the tuning process also explores configurations with 50 and 200 trees.
2. **Maximum Depth**: This hyperparameter specifies the maximum depth of each tree, defining the number of computational nodes allowed. The default value, 'None,' enables trees to grow until all leaves meet the minimum sample requirement for splitting. The tuning process includes fixed values of 10, 20, and 30.
3. **Minimum Samples to Split**: This defines the minimum number of samples required to split a tree node. The default value is 2, but values of 5 and 10 are also tested during the optimization process.
4. **Minimum Samples per Leaf**: This parameter sets the minimum number of samples needed to form a leaf node. The default value is supplemented by options of 2 and 4 to determine its influence on model generalization.
5. **Maximum Features for Splitting**: This hyperparameter dictates the maximum number of features considered when identifying the optimal split. Options include considering all features (n), the square root of n, and the binary logarithm of n.

Throughout the tuning process, cross-fold validation with 5 folds (k = 5) was employed to enhance the model's robustness across various subsets of the training data. The r2 scoring metric was employed to train the model, focusing on the ability to explain variance in the target variable effectively.

Part IV

RESULTS EVALUATION

How well do the proposed methodologies perform?

6. Results of the methodologies

This section presents the results of both methodologies employed. In the first subsection, which is reserved for the outcomes of the engineering approach, hygrothermal performance and distribution of degradation risks across Facade 1 is presented. The subsection concludes by highlighting correlations between the FTDR index and WDR, solar and longwave radiation. The second subsection highlights the outcomes of the Data-driven approach. Specifically, results for the two experimental setups including the two hold-out samples are presented.

6.1 Engineering approach

The implementation of the engineering approach involved 31 years (1991-2022) of hygrothermal simulations for 104 sections. The difference in hygrothermal performance across the facade is illustrated on two points with distinct boundary conditions. These are positioned below the roof overhang (Point A) and in the middle of the brickwork (Point B) as Figure 19 shows.

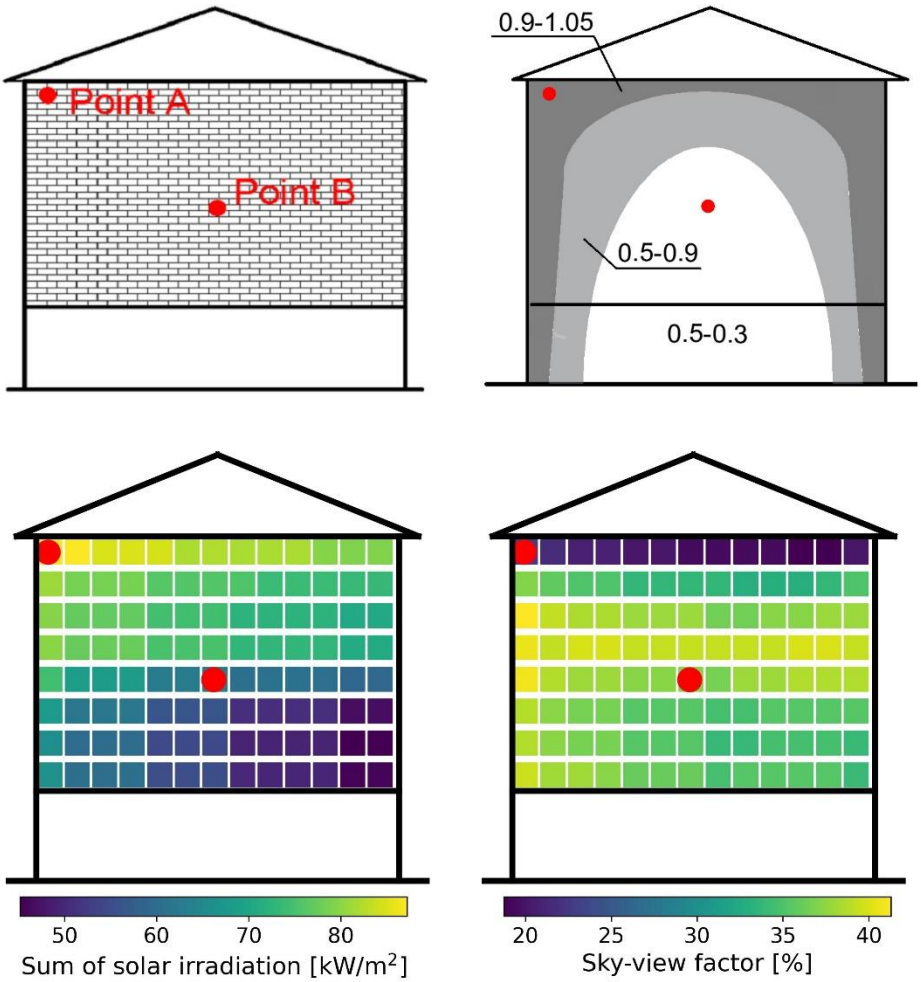

Figure 19 Position of the examined points for illustrating difference in hygrothermal performance (red points) and summary of weathering impact. The top left image shows the position of examined point. The top right relates the points to the Rain admittance factor. The bottom left illustrates the sum of solar irradiation across the 104 sections of the facade over all winter months of the 31 years period. The bottom right shows the distribution of the sky-view factor over the facade.

Point A and B can be regarded as the opposite extremes in terms of their WDR exposure. The RAF coefficient of the former point is the highest across the facade (1.02). On the contrary, the latter point is associated with one of the lowest RAF coefficients (0.4). In terms of their total solar radiation exposure over all winter months of the simulation period, Point A is, despite the presence of roof overhang, the most exposed spot on the facade, totaling almost 90 kW/m^2. From this point, the total irradiation gradually decreases towards the bottom right corner, thus Point B is moderately exposed with 65 kW/m^2. Finally, the sky-view factor reflects the presence of the roof overhang, rendering Point A, and the other sections at the height, the least exposed point in terms of sky radiation cooling (22%). Point B is in this regard much more exposed, exhibiting 37% of the view to be open towards the sky. How these differences translate into subsurface hygrothermal performance is illustrated in Figure 20, presenting a period from January to March of 1995. The year was chosen as a representative year as its winter mean temperature is closest to the mean winter value for all 31 simulation years.

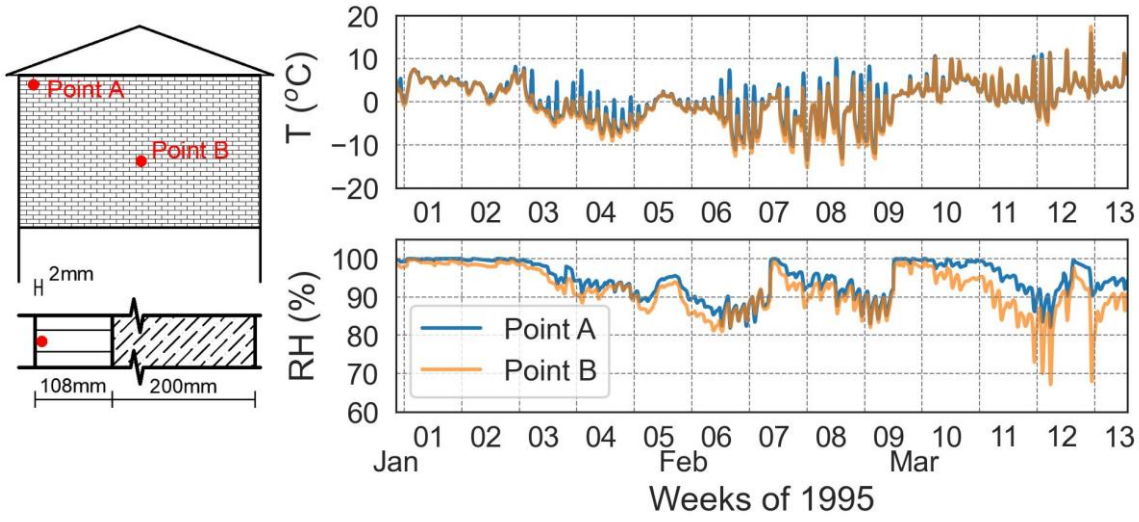

Figure 20 Hygrothermal performance 2 mm below the facade surface of Points A and B over the first three months of 1995. The top graph shows the progression of temperatures. The bottom depicts the progression of relative humidities.

As illustrated, both points demonstrate similar temperature profiles, with Point A being slightly warmer than Point B due to the presence of more pronounced peaks and slightly shallower valleys. These differences, which can be attributed to the effects of solar and sky radiation, and particularly the peaks impact the number of times the subsurface temperature falls below 0°C. This can be observed especially during the third and the fourth week of the examined period, but a few instances can be observed in the sixth and the ninth week. In general, freezing and thawing cycles are scarce in the first two weeks of the examined period. This is followed by two weeks when Point A is subjected to nine cycles while Point B to 3. After a brief thaw, a cold period from the sixth week to the tenth week exerts numerous cycles on both points. During this period, both points exhibit their minimum temperatures with -13.5 and -15.33 °C for Point A and Point B, respectively.

A comparison of relative humidities for the two points reveals more noticeable differences, with Point A exhibiting higher levels of moisture saturation. This reflects WDR boundary conditions, where the adversity is more pronounced in the corners of the facade as illustrated in Figure 19. Nevertheless, both points exhibit either complete or nearly complete saturation in the beginning of the period examined but start getting drier from the third week. The drying process is occasionally intercepted by rain events of different intensities. For instance,

both profiles peak again in the seventh and the ninth week. Interestingly, the occurrence of the minimum relative humidity for the points differs significantly with Point A recording its minimum (81.9 %) in the sixth week and Point B (67.1 %) in the twelfth week of the examination period. Inherently, the difference in temperatures and relative humidities between the points result in a distinct freezing and thawing performance which is illustrated in Figure 21.

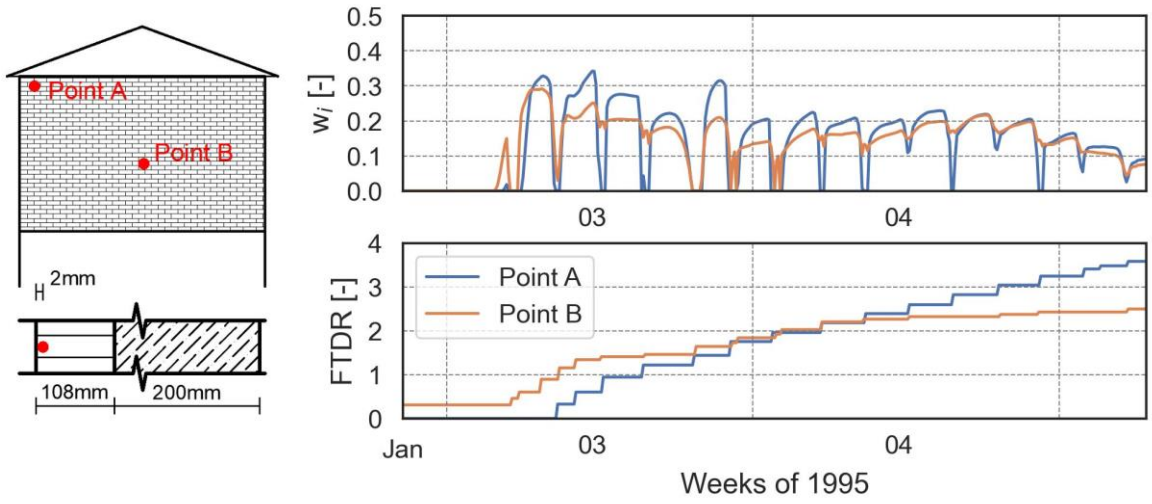

Figure 21 Comparison of freezing-thawing performance 2 mm below the outer surface between points A and B during the third and fourth week of 1995. The top graph shows the formation of ice measured by the saturation degree of ice content (w_i). The bottom graph shows the cumulative sum of the differences between the minimum and maximum w_i in each complete and incomplete freeze-thaw cycle, which is known as the FTDR index.

As shown during the third and fourth weeks of 1995, Point A is exposed to more complete freeze-thaw cycles than Point B. In contrast, Point B remained frozen for most of the period, undergoing fewer complete cycles but more incomplete ones. Specifically, Point A was subjected to 10 complete and 4 incomplete freeze-thaw cycles, whereas Point B is exposed to 6 complete and 12 incomplete cycles. The maximum ice saturation degree reached 0.34 at Point A and 0.29 at Point B.

These differences influence the FTDR index over time. By the end of the examined period the FTDR index, which is calculated at the end of every complete and incomplete freezing and thawing cycle, reached 3.59 at Point A, compared to 2.19 at Point B. Notably, Point B had been already subjected to a freezing condition earlier that year, starting the two-week period with FTDR index of 0.16. Extending the period, further deepens the disparity between the points. This is illustrated in Figure 22, which compares the FTDR index for these points and all other sections of the facade over the entire 31-year simulation.

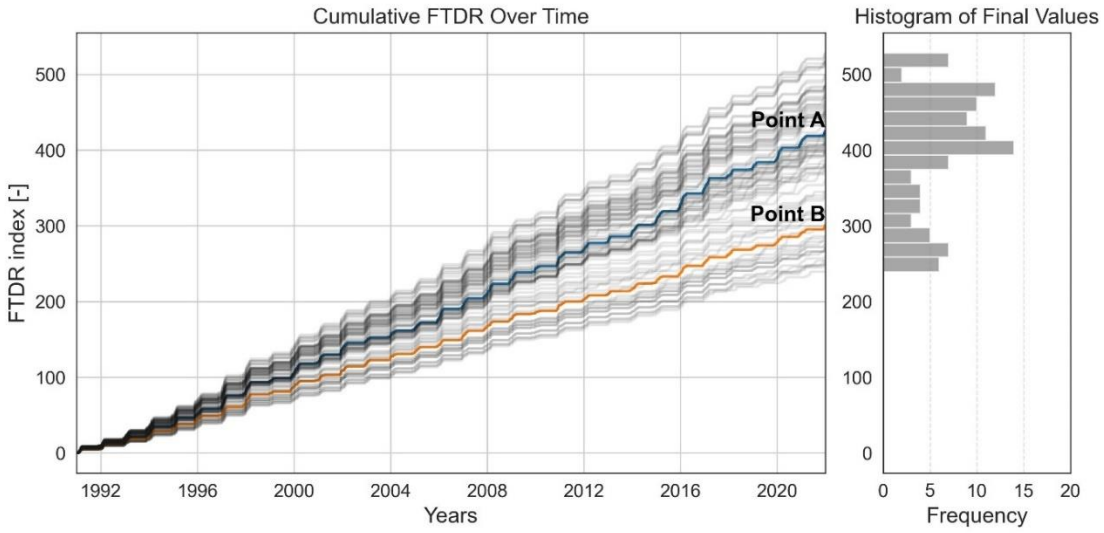

Figure 22 Progression of FTDR index for all facade sections. On the left, the graph illustrates a cumulative FTDR for all sections over the period of 1991 to the end of 2021, highlighting Point A and Point B. On the right, the histogram shows the frequencies of the final FTDR values.

As observed, the FTDR indices for all facade sections progress in a linear fashion and differ considerably by the end of the simulation period. The recorded FTDR index ranges from a maximum of 528.3 to a minimum of 239.4. In this context, the final FTDR index for Point A resulted in 424.0, which is near the median value of all outcomes (411.2). In contrast, the FTDR index for Point B fell within the first quartile, concluding at 300.3.

The slope of the FTDR progression, and consequently the final FTDR index for each section, is primarily driven by the severity of its boundary conditions. To better understand the impacts of the weathering factors, scatter plots showing the relationship of the FTDR index to Rain Admittance factor (RAF), winter mean solar radiation, and sky-view factors are presented in Figure 23. To emphasize the relationships, data are fitted using second-degree polynomial regression. The analysis is performed separately for sections adjacent to the roof overhang and to other sections, due to their observably distinct performance.

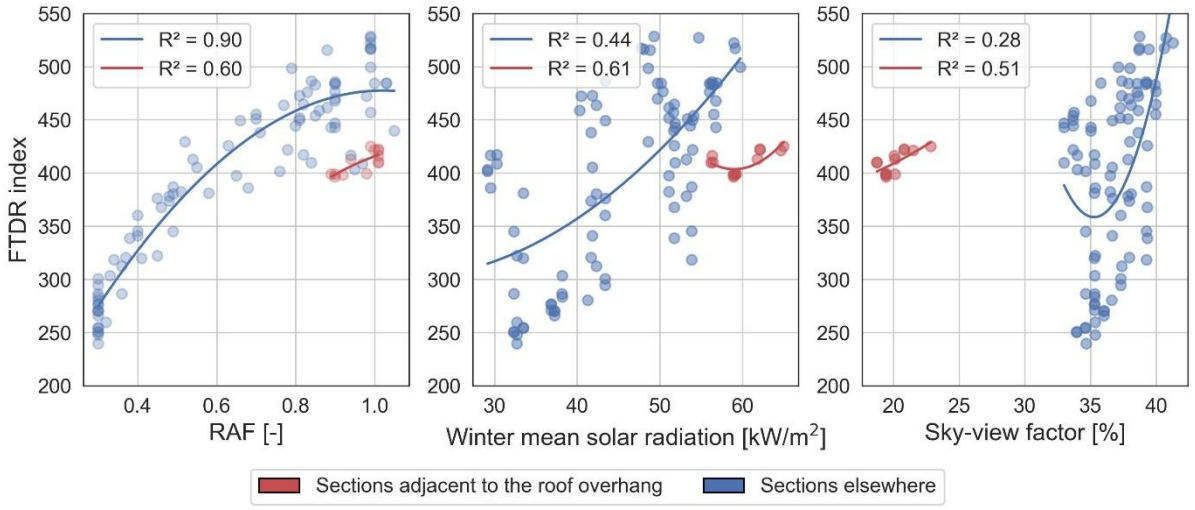

Figure 23 Scatter plots comparing the relation between the FTDR index and RAF (on the left), winter mean solar radiation (in the middle) and the sky-view factor (on the right). Correlation analysis is done separately for sections positioned directly below the roof overhang (red color) and other sections (blue color). Each sample is fitted with the second-degree polynomial regression curve.

As illustrated, sections not adjacent to the roof overhang show a meaningful polynomial regression fit only in the case of the RAF coefficient, indicating that Wind-Driven Rain (WDR) is the most influential variable. Its R-squared (R^2), the most common method for evaluating the fit of regression curve, is 0.90. Other weathering factors show a weak to negligible relationship with the FTDR index, though winter mean solar radiation explains 43% of the variance (R^2 = 0.44), indicating some influence. In contrast, sections directly below the roof overhang demonstrate stronger relationships between the FTDR index and weathering factors. Specifically, RAF and winter mean solar radiation account for 60% (R^2 = 0.60) and 61% (R^2 = 0.61) of the variance in the FTDR index, respectively.

The results from the application of the engineering approach on Facade 1 are further complemented in Section 7.1. There the FTDR index is mapped in sections across the facade and compared to the actual degradation derived in Section 3.

6.2 Data-driven approach

The predictive capabilities of the Data-driven approach are tested in the context of the two experimental setups, which are defined in the Section *5.2.2*. Performance is assessed using two distinct samples:

1. **Test Hold-Out Sample** – This comprises 20% of the data from 15 facades and is used to evaluate the algorithm's ability to predict degradation ratios for facades drawn from the same distribution as the training set.

2. **Validation Facade Sample** – This sample consists of facades that were excluded from training to test the model's generalization ability on degradation patterns that may not follow the same distribution as the training data.

This evaluation framework ensures a thorough assessment of the model's predictive performance across both familiar and unseen facade conditions.

6.2.1 Set-up 1 – automatic feature selection

The threshold for the inclusion of a feature in the random forest regressor was derived by calculating the mean of the relative importance of all features and reads 0.059. Five features were further considered in the training process. These are listed in Table 5, which ranks all features based on their importances.

Table 5 Selection of features based on their importance as estimated by Random Forest regression algorithm. The feature selection threshold (0.059) is indicated by the dashed line.

	Feature	Importance
1	Sky-view factor	0.311
2	PCA rain 2	0.219
3	PCA rain 1	0.155
4	Height from ground	0.124
5	Distance to closest edge	0.060
6	160 ≤ Rain < 200	0.030
7	200 ≤ Rain < 240	0.029
8	240 ≤ Rain < 280	0.018
9	0 ≤ Rain < 40	0.015
10	120 ≤ Rain < 160	0.014
11	Rain sum	0.009
12	Rain mean	0.008
13	80 ≤ Rain < 120	0.004

14	Facade constant	0.003
15	40 ≤ Rain < 80	0.001
16	280 ≤ Rain < 320	0.000
17	320 ≤ Rain < 360	0.000

As observed, the training process included the three elementary features, namely the sky-view factor, height from the ground and the distance from the closest corner. These are complemented by the two principal components derived from azimuth-based rain features. The training of the random forest regressor and the optimization using cross-fold validation, resulted in a set of following hyperparameters:

- **Number of Trees**: 200
- **Maximum Depth**: N/A
- **Minimum Samples to Split**: 2
- **Minimum Samples per Leaf**: 1
- **Maximum Features for Splitting**: sqrt

The application of the tuned model to the test sample and the validation facade is shown in Figure 24.

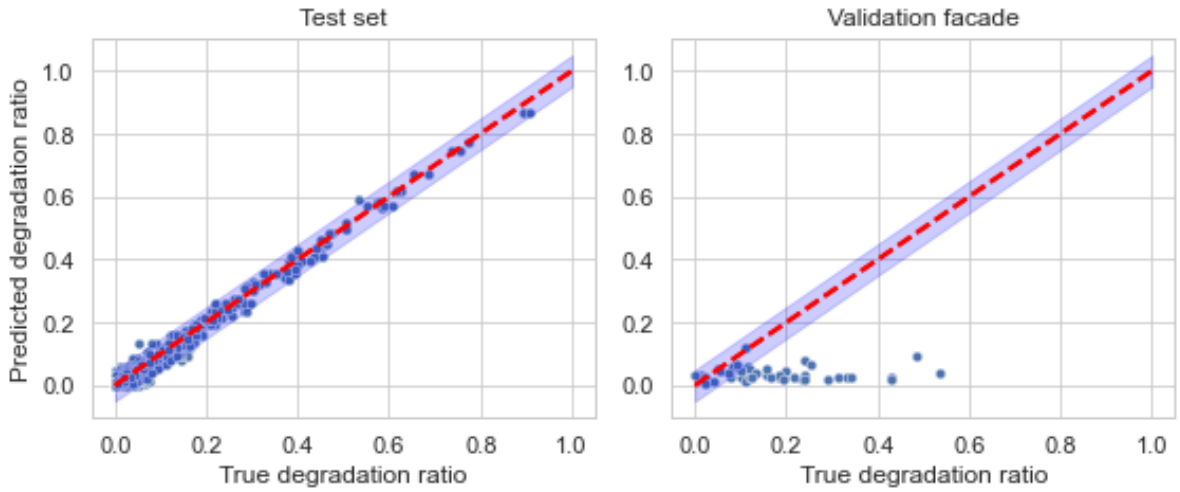

Figure 24 Application of Random Forest regressor on the test set (to the left) and on the validation facade (to the right), using features selected in Table 5. The plots illustrate the comparison between predicted and actual degraded/undegraded ratio in each section of the facade. The red dashed line represents the theoretical best possible agreement between the predicted and actual values.

For the test hold-out sample, nearly all predictions align closely with the red dashed line, which represents the ideal best-fit between actual and predicted degradation ratios. This strong model performance is reflected in an R^2 value of 0.978. However, predictions for the validation facade tend to be lower overall, with the highest estimated degradation ratio reaching only 0.12. The poor performance on the validation sample is evident from the R^2 value of -1.152.

6.2.2 Set-up 2 – manual feature selection

This experimental set-up tests different feature combinations to assess their impact on predictions over the validation facade. Three elementary features from Set-up 1, i.e., sky-view factor, height above ground, and distance from the nearest edge, are kept constant throughout the analysis. These are complemented by the inclusion of “Facade constant” in the feature space. Although this feature showed low estimated importance in Set-up 1 (

Table 5), its inclusion is justified, as the presence of a ventilated cavity is known to significantly influence the hygrothermal performance of facades and, consequently, the occurrence of degradation. Moreover, its importance within the random forest regression may increase when combined with specific feature subsets. The primary focus, however, is on the azimuth-based features, which are modified in each iteration.

To illustrate their influence on predictive performance, three examples are considered:

1. The feature 0 ≤ Rain < 40,
2. The feature 200 ≤ Rain < 240,
3. A combination of two azimuth-based features: 0 ≤ Rain < 40 and 160 ≤ Rain < 200.

Regardless of the feature selection, hyperparameters are optimized, and the algorithm is trained as described in Section 5.2.3. Figure 26 shows the performance of the model using the three sets of features evaluating both test and validation hold-out samples.

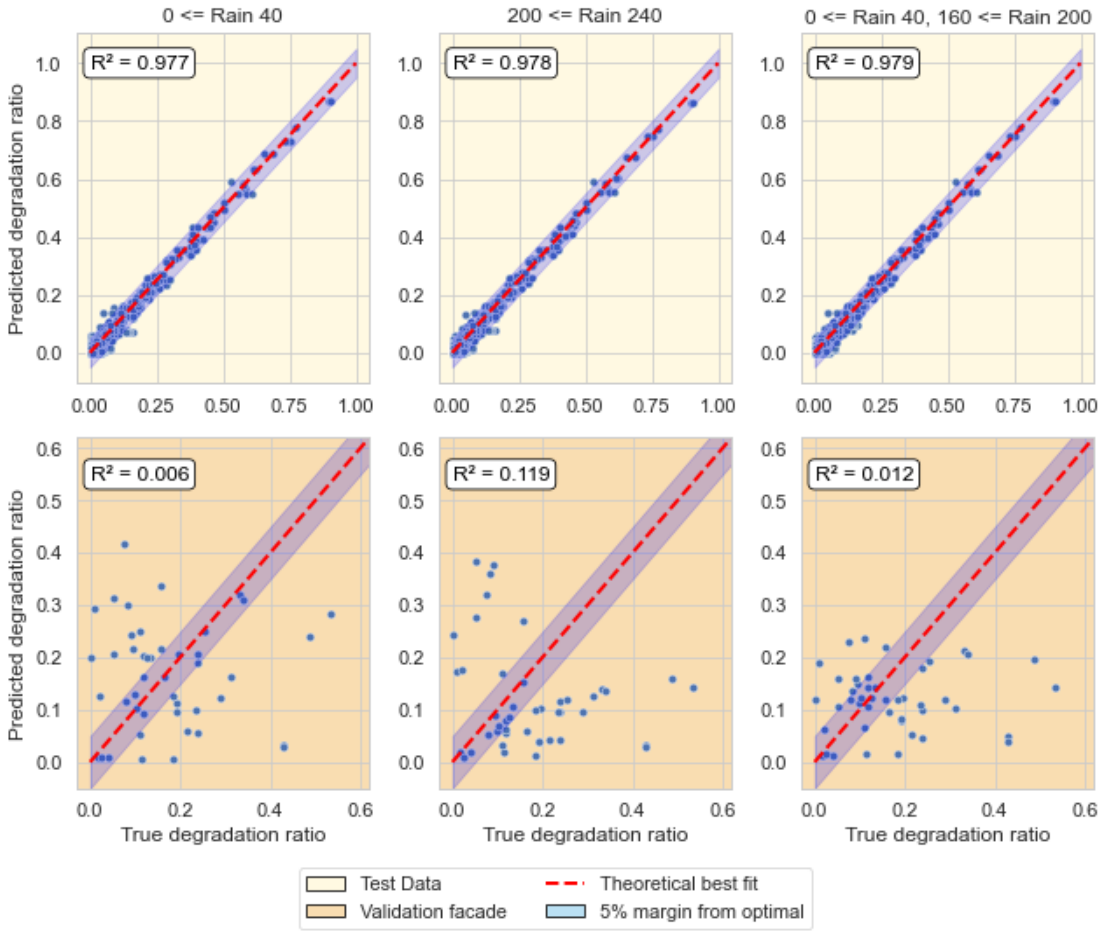

Figure 25 Application of the Random Forest regressor on the test set (first row) and the validation facade (second row) using three different subsets of azimuth-based features: (1) 0 ≤ Rain < 40 (left), (2) 200 ≤ Rain < 240 (middle), and (3) a combination of 0 ≤ Rain < 40 and 160 ≤ Rain < 200 (right). Each model also includes three elementary features: sky-view factor, height above ground, and distance from the nearest edge, and the Facade constant. The red dashed line represents the ideal agreement between predicted and actual values.

As observed, using different, manually defined feature subsets, yields insignificant performance differences in the test sample but exerts notable performance changes in the validation facade. The application of the models on the test sample resulted in nearly identical

performance across the cases, reaching the minimum R^2 value of 0.977, which is also practically the same as the case presented in Set-up 1 (R^2 = 0.978).

While the model in Set-up 1 consistently underpredicted degradation ratios (with a maximum prediction of 0.12), the three alternative models exhibited much greater variability, leading to both over- and underestimation. For instance, in the case using 0 ≤ Rain < 40, the highest predicted degradation ratio reached 0.42, while the corresponding actual value was only 0.07. Conversely, the model severely underpredicted degradation for another section, where the true value was 0.41, but the model estimated only 0.03. Overall, the model overestimated degradation in 14 out of 40 sections and underestimated an equal number.

Performance was similarly inconsistent across other feature subsets. The best overall r2 score (0.119) was achieved using 200 ≤ Rain < 240. However, the model that produced the fewest overestimations used the combined feature subset 0 ≤ Rain < 40 and 160 ≤ Rain < 200.

The results for the Validation facade in this experimental setup are further complemented in Section 7.2. There, the spatial distribution of predicted degradation ratios across the facade are compared to the actual distribution of degradation, which was derived in Section 3.

7. Comparison of predictions to target

In this section, the results of the two methodologies, i.e., the risk of degradation or its prediction across facades, are compared to the actual degradation state of the same facades.

7.1 Engineering approach

The implementation of the engineering approach on Facade 1 resulted in a long-term evaluation of freezing and thawing risks across its 104 sections. Hygrothermal response of each section was simulated over 31 years (1991-2022), and the freezing and thawing performance was evaluated using the Freeze-Thaw Damage Risk (FTDR) Index.

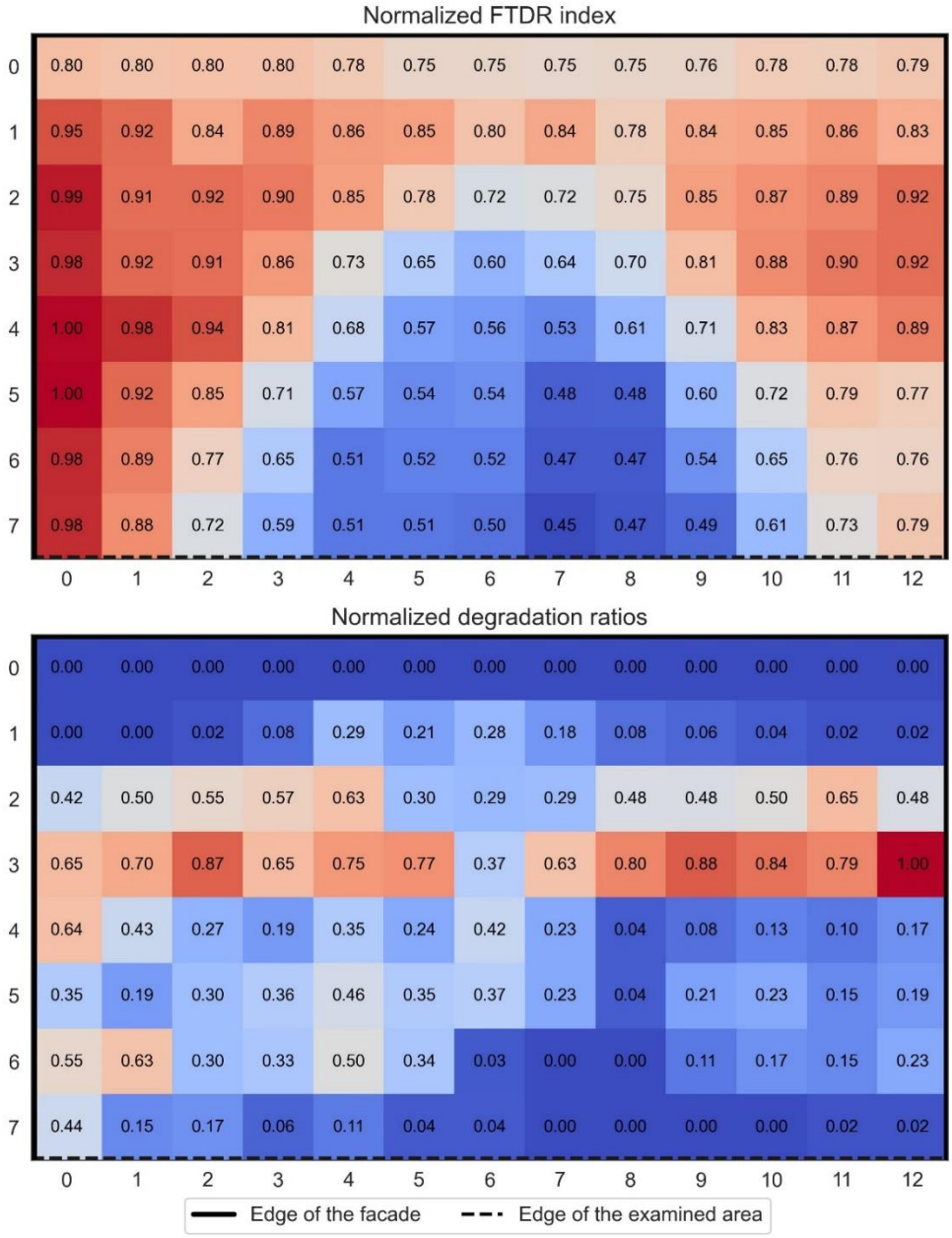

Figure 26 Spatial comparison of the FTDR index as derived by the engineering approach (top) and the actual degradation ratios (bottom). Values in both heatmaps are scaled against their respective maximums to ensure better comparability.

To assess the accuracy of the outcomes, the FTDR index in each of the 104 sections is compared to the corresponding degradation ratio, as obtained in Section 3. Comparing the risk and the degree of degradation is deemed appropriate as one should theoretically correlate to the other. However, to ensure direct comparison, both variables are scaled against their respective maximum. The comparison is performed by mapping the FTDR index and the degradation ratios to the facade sections as shown in Figure 26.

As observed, the distribution of the FTDR index across the facade does not correspond to the actual degradation. Instead, it closely follows the distribution of the RAF coefficient, as shown in Figure 19. This is expected, given the strong correlation between the RAF coefficient and the FTDR index (Figure 23). However, the influence of the other climate factors, i.e., solar radiation and longwave sky radiation, is also evident. Notably, a reduced sky-view factor in sections adjacent to the roof overhang lowered degradation risks by 20 to 25 %. Additionally, solar radiation, which is highest in the top left corner during winter and gradually decreases toward the bottom right corner (Figure 19), contributes to the variation in FTDR indices, with lower values observed in the bottom right sections.

The true distribution of the degradation across the facade exhibits markedly different pattern. Most noticeably, the degradation is manifested as a band that extends from the left to the right, situated above the central portion of the facade (row 2 and 3). Furthermore, the left side of the facade exhibits a more pronounced degradation, while areas below the roof overhang and at the bottom right are intact.

7.2 Data-driven approach

The outcomes of the random forest regressor trained within the Beyond (data-drive) approach and implemented onto the validation facade (Facade 2) are further mapped into the sections across the facade and compared with the actual degradation ratios derived in Section 3. This is done for the three cases of the experimental Set-up 1, which results were presented in Section 6.2.2. The actual degradation ration across the validation facade is shown in Figure 27.

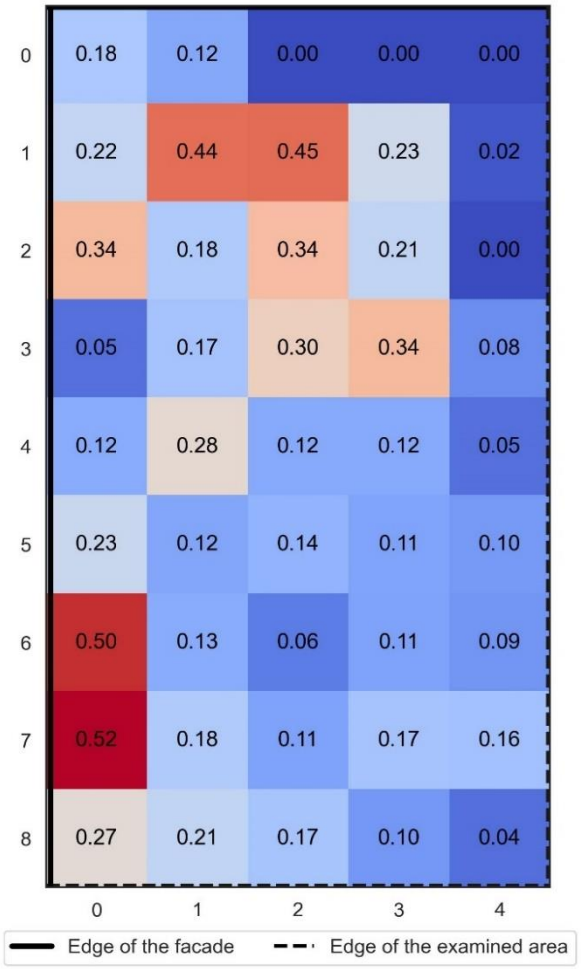

Figure 27 Distribution of actual degradation ratios over the validation facade. The values were derived based on computer vision analysis presented in Section 3.

As observed, the degradation is clustered above the center of the facade (rows 1 - 3) and near the edge of the facade, where the maximum degradation ratio is located (0.54). From these clusters, the degradation ratios get progressively lower towards the right edge of the examine area. This is apparent also in the sections adjacent to the roof overhang, which prevented degradation from occurring at columns 2 - 4. The true distribution of degradation over the validation facade is further compared to the outcomes of the three cases from Set-up 2. Figure 28 shows the degradation distributions as predicted by the random forest regressor.

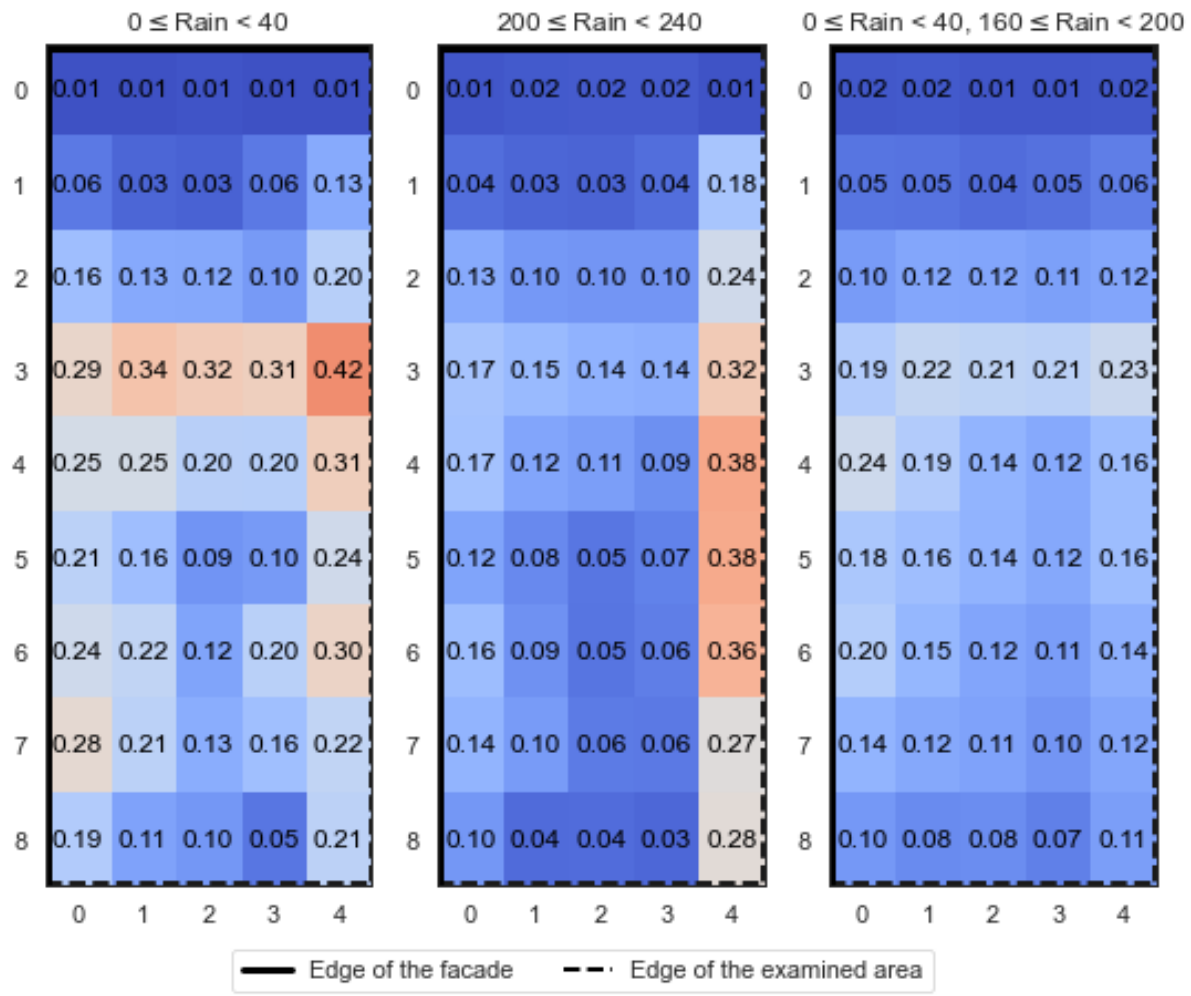

Figure 28 Spatial distribution of degradation predictions for three subsets of azimuth-based features. (1) 0 ≤ Rain < 40 (left), (2) 200 ≤ Rain < 240 (middle), and (3) a combination of 0 ≤ Rain < 40 and 160 ≤ Rain < 200 (right). Each model also includes three elementary features: sky-view factor, height above ground, and distance from the nearest edge, and the Facade constant.

The predictions based on different subsets of features exhibited distinct spatial patterns over the validation facade. The 0 ≤ Rain < 40 subset (left) produced a pattern that resembled the actual degradation distribution (Figure 27). However, deviations were particularly noticeable in the upper sections of the facade (rows 0–2), where actual degradation was most prevalent, reaching a maximum of 0.45. In contrast, the model underestimated degradation in this region, predicting a maximum of only 0.03. Further notable discrepancies are in column 4, which is almost entirely, except row 0, highly overestimated and includes the predicted maximum of 0.42.

A similar pattern can be observed when using 160 ≤ Rain < 200 (middle). However, in this case, the degradation ratios are generally less pronounced except for column 4 where some predictions are higher, reaching a maximum of 0.38.

To some extent the same pattern is discernable with the combined feature set (0 ≤ Rain < 40, 160 ≤ Rain < 200) employed (right). In this case, the degradation ratios steadily increase from the bottom right corner to the left corner of row 3.

Part V

SUMMARY

Applicability and outlook.

7. Discussion

This section focuses on setting the outcomes from the case studies into perspective, discussing the applicability and limitations of the two proposed methodologies.

7.1 Limitations of the engineering approach

As seen in Section 7.1, the implementation of the engineering approach on Facade 1 resulted in the distribution of degradation risks (FTDR index) across the facade that did not correspond to the actual facade degradation. This discrepancy may be attributed to uncertainties inherent to the methods used in the analysis to quantify the effects of microclimate across the facade. In particular, the effects of WDR across the facade, which has proven to be the most influential factor in the FTDR assessment (Figure 23), are captured using semi-empirical methods, which are known to be limited in facades with complex surroundings. Specifically in the case study, the Straube and Burnett (SB) method for WDR quantification was implemented for its quality to distinguish the effects of rain over a facade more finely compared to the other methods. Nevertheless, the other two methods, i.e., ISO 15927-3:2009 and ASHRAE 160, may have been more appropriate in addressing the specificities of the case study. The reason for this is twofold and include:

1. **Weather data scaling** – Unlike the standardized methods, the SB method does not incorporate coefficients for scaling rain and wind data from weather stations (or climate models) to the on-site specifics of the case study.
2. **Disregarding the roof overhang** – The used SB method allows to map WDR across several different facade geometries. The geometry used in the case study did not consider roof overhang, as shown in Figure 19.

The first reason is deemed critical for the success of the analysis. To illustrate, ISO standard includes coefficients to scale down WDR based on the distance to nearby obstructions and the terrain categories (e.g., urban, suburban). These could have lessened the effects of WDR over the outcomes, pronouncing the impact of other weathering factors. Ultimately, this could have led to more precise outcomes as the sky-view factor was shown to correlate well with the degradation ratios over Facade 1 (Figure 17). Nevertheless, even the employment of either ISO 15927-3:2009 or ASHRAE 160 still doesn't guarantee the success of the analysis as neither of the semi-empirical methods were developed to capture all complexities of the surroundings.

Interestingly, incorporating the roof overhang into the SB method could enhance the accuracy of degradation risks (FTDR) mapping across the facade. As further analysis of Figure 26 suggests, the actual degradation pattern over the facade aligns more closely to the modeling results when the results are shifted downward, away from the roof overhang. From the modeling perspective, this inverted U-shaped pattern stems from the RAF coefficient, which reflects the distribution of wind pressure over the facade. Adjusting the RAF mapping lower on the facade while assuming low RAF in sections close beneath the roof overhang could significantly improve the accuracy of the results. However, some inaccuracies are to be expected, as the RAF mapping in the SB method is based on wind acting at normal angle to the facade. This could be the worst-case scenario but may not represent well the true wind exposure of the facade in the complex environment with sheltering effects. Another source of uncertainty lies in material properties, which influence hygrothermal modeling and, consequently, the evaluation of the FTDR index.

Suitable technical documentation is often lacking, especially for older buildings, making it difficult to obtain precise material characteristics.

In this application of the Engineering approach, material properties were sourced from the WUFI material database, while specific values used for FTDR index calculations were obtained from other references. However, the use of the FTDR index is not mandatory in the Engineering approach. Instead, the number of freezing and thawing cycles could have been used to maintain consistency with material databases and avoid potential discrepancies.

Additionally, general surface boundary conditions—such as the rainwater absorption factor, which determines the fraction of impacting rain available for capillary suction—must be approximated due to limited data availability.

7.2 Limitations of the Data-driven approach

The two experimental set-ups provided key insights. First, the methodology effectively identifies areas under significant environmental stress, making them more susceptible to degradation. This is supported by the test hold-out sample, where the random forest regression model estimated most degradation ratios with a margin of error below 5%.

However, applying the model to the validation facade reveals a crucial limitation for practical implementation. Unlike the test hold-out sample, which was drawn from the same distribution as the training data, the validation facade was reserved for later testing. The inaccurate predictions on the validation sample likely result from a distribution shift, a well-documented challenge in machine learning applications.

In essence, the distribution shift prevents the model from generalizing effectively to unseen data. A useful analogy is a self-driving car trained and successfully tested on the wide streets of Gothenburg, Sweden, but then deployed in the narrower, less familiar streets of Thessaloniki, Greece. Similarly, the validation facade presents environmental conditions and degradation patterns that differ from those in the training and test sets, leading to reduced model performance. This aligns with the observations in Section 3, where Figure 9 and Figure 10 illustrate that degradation patterns vary uniquely across facades. In other words, the model has likely learned patterns specific to the training set, which do not fully translate to the validation facade.

Moreover, distribution shift can affect both the predictive power of features and their selection. A feature that demonstrates high predictive potential across most facades may become irrelevant or even misleading when applied to facades with distinct degradation patterns. This shift also explains the prediction sensitivity observed in the validation facade when using different feature subsets, as illustrated in Figure 25. In conclusion, addressing the distribution shift is essential for the further development of the methodology. Presently, the shift stems from two limitations:

1. **Insufficient training sample** – The current database consists of 16 facades, but many similar buildings across Sweden could be added. Expanding the dataset to include facades with degradation patterns like the validation facade may help reduce the distribution shift gap.
2. **Insufficient incorporation of renovation history** – Renovation history was accounted for only superficially. Most buildings in the dataset were constructed in the early 1960s, with one exception from 1954. Despite their long lifespan, efforts to document facade

renovations yielded limited information—the earliest recorded renovation dates to 2011. In such cases, newly replaced bricks are often distinguishable by their brighter color. However, a closer inspection of several facades reveals additional areas where brickwork appears distinct from the rest. The challenge lies in determining whether these variations are due to previous replacements or other factors, such as differences in material properties from a separate batch of bricks. Given these uncertainties, the degradation analysis focused only on visibly damaged bricks and those with significantly brighter color. However, this approach likely imposed limitations, as it may have led to an oversimplified degradation pattern.

Whereas the first limitation is easily addressable as more and more facades can be added into the database, the second point requires a significant improvement of the computer vision algorithm used in the analysis. The current approach relies on a supervised computer vision algorithm, which identifies patterns based on predefined annotations. However, this method has limitations when detecting unlabeled deviations in brickwork.

A more effective alternative could be an unsupervised machine learning approach, such as the k-means algorithm, which clusters bricks based on deep computer vision features. This technique could categorize bricks into clusters representing damaged areas, replacements from 10 years ago, older repairs, and so on. The number of clusters (k) could be user-defined or determined automatically by the algorithm. Additionally, integrating non-destructive testing methods could enhance accuracy, leading to a more comprehensive degradation analysis. Ultimately, this refined approach could produce significantly different insights and potentially address the distribution shift issue.

Narrowing the distribution shift gap would enhance the methodology's ability to identify facade sections under failure conditions and predict potential degradation risks. Additionally, it could help determine which areas are more susceptible to severe damage over time. However, for a more precise understanding of degradation onset, it is essential to consider facade composition and material properties. For example:

- Drying potential: Some facades facilitate better moisture evaporation, delaying degradation.
- Moisture tolerance: Certain brick types can absorb more moisture before reaching saturation, postponing freeze-thaw damage.
- Material variability: Properties may differ within the same facade, affecting degradation patterns.

To account for these factors, the degradation ratio of each section could be scaled using Monte Carlo-based hygrothermal simulations. This would estimate how many freeze-thaw cycles a facade must endure before deterioration begins. Ultimately, this approach would improve predictive accuracy, helping determine when and to what extent degradation is likely to occur.

7.3 Applicability of the methodologies

The two methodologies are fundamentally different to each other, using different methods and tools that—as discussed above—are bound to distinct limitations. Naturally, their predictive power differs as well as their applicability. Table 6 compares the two methodologies in terms of time complexity, accuracy, interpretability and scalability.

Table 6 Comparison of the two methodologies in terms of their applicability

Criteria	Engineering approach	Data-driven approach
Accuracy *	Low	Low
Interpretability	High	Moderate
Preparation time	Long	Long at first - reducing over time **
Application time		Short
Scalability	Low	High

* Both methodologies showed low accuracy in case study facades 1 and 2, respectively. Nevertheless, they both can be improved significantly

** Including the application of Framework for degradation analysis

Each domain of the applicability given in the Table 6 —except accuracy, which was presented and discussed above—is further discussed separately.

7.3.1 Interpretability

Although both methodologies aim to assess the risk of moisture induced degradation across facades, each uses different metrics to present their outcomes.

Engineering approach uses performance indicators—FTDR index in the case study—that are commonly used in hygrothermal assessment. Such indicators express the risk of degradation in relative terms, comparing sections to each other. Ultimately, more freezing and thawing cycles mean a higher risk of degradation.

The Data-driven approach estimates the risk of degradation by directly predicting the ratio of degradation for each facade section. Ideally, these direct predictions should be held as definite and inevitable, as predictions are drawn from other facades that exhibit deterioration. However, it must be stressed that they are not so, primarily because of the discussed uncertainties regarding renovation history of the facades. As a result, the predicted degradation ratio might be a mix of data drawn from facades that are at different stages of their life cycle. Therefore, the outcomes from the Data-driven approach must be at the present regarded as microclimate indicator, showing where the facade is likely to degrade due to environmental impacts.

7.3.2 Time complexity

The application of each methodology on a facade is undertaken using a different application paradigm. Engineering approach is applicable to one facade at a time, making the time for the preparation and application of the methodology inseparable. On the other hand, Data-driven approach requires a database—integrating degradation data with spatial and weather data—and a trained machine learning predictor to perform any predictions. This separates the time needed for the preparation of the methodology and time for its application.

The time investments needed to apply the Engineering approach can be characterized as substantial in general. The computational costs depend mainly on two factors. The first factor is the number of sections to analyze. Defining the resolution of the outcomes, it predefines the computational expenses of the entire undertaking. The second factor that defines computational costs is the simulation time.

To exemplify the computational costs, the case study performed in this thesis featured 104 facade sections, performing 31 years of hygrothermal simulation. Several hours were spent defining boundary conditions, most of which were taken to perform irradiation analysis, followed

by the arrangement of boundary conditions into 104 WUFI models. Hygrothermal simulation itself took nearly 10 hours to perform on Intel(R) Core(TM) i9-10900 CPU @ 2.80GHz 2.81 GHz. Finally, the last substantial time investment (several hours) was the collection of data from the WUFI hygrothermal models. It must be noted that the whole process was also very labor intensive.

Time complexity of the Data-driven approach primarily stems from its preparation phase. Substantial time and effort must be put into building suitable computer vision algorithms, mining features from a 3D-model of the neighborhood, finding optimal feature space and constructing a machine learning predictor. When these are done, however, it takes only to mine the required features to make predictions.

In the context of the presented case study, the (re)training of the computer vision framework to detect damaged and replaced bricks took dozens of hours. This process included data collection, image annotations, the training process itself, manual inspection and sometimes correction of false detections. The process of mining data from a 3D model required a Grasshopper function, which development took several hours, but which can collect data almost instantaneously. Finally, the largest portion of time took the development machine learning predictor, respectively the testing the impact of individual features on the outcomes.

7.3.3 Scalability

Scalability is closely related to the time complexity of the methodologies. Applying the Engineering approach to a facade always requires completing its three steps defined in Section 4, making its potential application to many facades a cumbersome endeavor. On the contrary, once all the methods and tools of the Data-driven approach are prepared and performing well in terms of their predictive capabilities, then the application of the methodology is nearly instantaneous. Moreover, further automation of the mining process of the features from a 3D-model would allow a quick assessment of facades within entire neighborhoods.

8. Conclusion and future research work

This section presents the concluding remarks of this thesis and offers an outlook on future research directions.

8.1 Conclusions

This thesis develops and evaluates two methodologies—Engineering approach and Data-driven approach—for assessing moisture-related risks across entire facades. These methodologies offer tools that bypass CFD-based simulations due to their practical limitations and enable the study of microclimate influences on degradation. Their primary application, as demonstrated in this thesis, is to identify where degradation is likely to occur on facades. Additionally, they can be used to analyze key driving factors and contribute to more effective conservation strategies.

To assess the accuracy of the proposed methodologies, the thesis applies them to 16 case study facades from existing buildings as part of an empirical validation. In this process, the proposed Framework for Degradation Analysis over Facades is employed to capture both the extent of degradation and its spatial characteristics across the facades. The degradation data reveals that south-facing facades exhibit significantly more damage than those with other orientations and that degradation does not follow any specific pattern. These data are then used to validate the two methodologies. Due to its labor-intensive nature, the first methodology is validated on a single facade, while the second is assessed using data from 15 facades with one additional facade reserved for independent validation.

The Engineering approach was applied to Facade 1 for being identified in the degradation analysis as the most severely damaged. The results showed discrepancies between the predicted degradation risks mapping and the observed degradation pattern, highlighting the limitations of readily available tools for practitioners to assess microclimate-based degradation risk. Based on the validation results, the primary cause for the discrepancies stems from the WDR quantification over the facade, which is handled in the case study using the SB method, which was chosen for its ability to finely distinguish WDR intensities across a facade. Nevertheless, the mapping of the modeled risk of degradation onto the facade suggested that moving the SB method's results down the facade—to account for the roof overhang—would lead to a relatively good agreement between the modeled predictions and observed degradation patterns.

The Data-driven approach was applied on all 16 facades in the case study to demonstrate its capabilities and the challenges of estimating the degradation patterns caused by microclimate. By using degradation data as the target variable and combining spatial data from a 3D neighborhood model with climate data as explanatory variables, the correlation analysis revealed no clear relationship across the sample, underscoring the difficulty of linking microclimate factors to degradation patterns. The random forest regressor model for predicting facade degradation showed excellent performance using the test dataset (a subset of 15 facades), achieving R-squared (R^2) value of 0.978. However, its performance dropped significantly (R^2=-1.152) when tested on the validation facade (Facade 2), which was initially excluded from the analysis. This discrepancy is attributed to the distribution shift—where the algorithm learns degradation patterns from the training data that do not generalize to the validation facade.

The applicability of both methodologies in practice requires different sets of tools and expertise, making both approaches time consuming to implement. However, the Data-driven approach has an undisputable advantage over the Engineering approach since its application will become less time consuming over time. Ultimately, the Data-driven approach could offer a computationally inexpensive way to assess facades in entire neighborhoods.

8.2 Future research

Both methodologies showed a potential in assessing the risk of degradation across entire facades. Nevertheless, both methodological approaches need improvements to be applied reliably in practice, addressing their discussed limitations. The Data-driven approach will benefit from expanding the training dataset and better incorporating the renovation history of facades. Capturing more degradation data over facades could narrow the observed distribution gap. The engineering approach on the other hand could be improved by modifying the SB rain quantification method to better account for the roof overhang. In theory, this can be done by using the results of ray-tracing analysis to scale down the WDR near small construction elements, as demonstrated for the ISO standard in [26].

Apart from improving the methodologies, both approaches could also potentially complement each other in future research. The Engineering approach may benefit from degradation observations and the correlations between degradation and climate-related features identified by the Data-driven approach. This integration could help refine its microclimate model, leading to more accurate boundary conditions for different sections across facades. Conversely, the Data-driven approach could leverage insights from the Engineering approach, incorporating physics-based features to enhance predictive performance of its machine learning model.

This thesis focused on identifying where degradation is likely to occur on facades. Future research could build upon this by incorporating a time dimension into the methodologies, addressing when degradation is likely to begin and how it may progress over time. This could be explored through various approaches, such as Bayesian theorem or Markov chains for state predictions. By bridging spatial and time aspects, these advancements could contribute to more proactive and effective conservation strategies.

References

[1] COMMUNICATION FROM THE COMMISSION TO THE EUROPEAN PARLIAMENT, THE COUNCIL, THE EUROPEAN ECONOMIC AND SOCIAL COMMITTEE AND THE COMMITTEE OF THE REGIONS A Renovation Wave for Europe - greening our buildings, creating jobs, improving lives. 2020. Accessed: Mar. 15, 2023. [Online]. Available: https://eur-lex.europa.eu/legal-content/EN/TXT/?uri=CELEX%3A52020DC0662

[2] M. Jerman and R. Černý, "Effect of moisture content on heat and moisture transport and storage properties of thermal insulation materials," Energy Build., vol. 53, pp. 39–46, Oct. 2012, doi: 10.1016/j.enbuild.2012.07.002.

[3] L. D. Hung Anh and Z. Pásztory, "An overview of factors influencing thermal conductivity of building insulation materials," J. Build. Eng., vol. 44, p. 102604, Dec. 2021, doi: 10.1016/j.jobe.2021.102604.

[4] S. Rouchier, M. Woloszyn, G. Foray, and J.-J. Roux, "Influence of concrete fracture on the rain infiltration and thermal performance of building facades," Int. J. Heat Mass Transf., vol. 61, pp. 340–352, Jun. 2013, doi: 10.1016/j.ijheatmasstransfer.2013.02.013.

[5] G. Eleftheriadis and M. Hamdy, "Impact of building envelope and mechanical component degradation on the whole building performance: a review paper," Energy Procedia, vol. 132, pp. 321–326, Oct. 2017, doi: 10.1016/j.egypro.2017.09.739.

[6] G. Eleftheriadis and M. Hamdy, "The Impact of Insulation and HVAC Degradation on Overall Building Energy Performance: A Case Study," Buildings, vol. 8, no. 2, Art. no. 2, Feb. 2018, doi: 10.3390/buildings8020023.

[7] G. Sullivan, R. Pugh, A. P. Melendez, and W. D. Hunt, "Operations & Maintenance Best Practices - A Guide to Achieving Operational Efficiency (Release 3)," PNNL-19634, 1034595, Aug. 2010. doi: 10.2172/1034595.

[8] I. Flores-Colen and J. de Brito, "A systematic approach for maintenance budgeting of buildings façades based on predictive and preventive strategies," Constr. Build. Mater., vol. 24, no. 9, pp. 1718–1729, Sep. 2010, doi: 10.1016/j.conbuildmat.2010.02.017.

[9] L. Thuvander, P. Femenías, K. Mjörnell, and P. Meiling, "Unveiling the Process of Sustainable Renovation," Sustainability, vol. 4, no. 6, Art. no. 6, Jun. 2012, doi: 10.3390/su4061188.

[10] K. Mjörnell, J. Arfvidsson, and E. Sikander, "A Method for Including Moisture Safety in the Building Process," Indoor Built Environ., vol. 21, no. 4, pp. 583–594, Aug. 2012, doi: 10.1177/1420326X11428340.

[11] A. Hukka and H. A. Viitanen, "A mathematical model of mould growth on wooden material," Wood Sci. Technol., vol. 33, no. 6, pp. 475–485, Dec. 1999, doi: 10.1007/s002260050131.

[12] N. W. Portal, A. W. M. van Schijndel, and A. S. Kalagasidis, "The multiphysics modeling of heat and moisture induced stress and strain of historic building materials and artefacts," Build. Simul., vol. 7, no. 3, pp. 217–227, Jun. 2014, doi: 10.1007/s12273-013-0153-4.

[13] M. Uranjek and V. Bokan-Bosiljkov, "Influence of freeze–thaw cycles on mechanical properties of historical brick masonry," Constr. Build. Mater., vol. 84, pp. 416–428, Jun. 2015, doi: 10.1016/j.conbuildmat.2015.03.077.

[14] I. Netinger Grubeša, M. Vračević, J. Ranogajec, and S. Vučetić, "Influence of Pore-Size Distribution on the Resistance of Clay Brick to Freeze–Thaw Cycles," Materials, vol. 13, no. 10, Art. no. 10, Jan. 2020, doi: 10.3390/ma13102364.

[15] J. Yue et al., "Study on Deterioration of Gray Brick with Different Moisture Contents under Freeze–Thaw Environment," Materials, vol. 15, no. 5, Art. no. 5, Jan. 2022, doi: 10.3390/ma15051819.

[16] B. Funk et al., "Impact of freeze–thaw weathering on integrity, internal structure and particle release from micro- and nanostructured cement composites," Environ. Sci. Nano, vol. 6, no. 5, pp. 1443–1456, May 2019, doi: 10.1039/C8EN01397G.

[17] Á. Török and B. Szemerey-Kiss, “Freeze-thaw durability of repair mortars and porous limestone: compatibility issues,” Prog. Earth Planet. Sci., vol. 6, no. 1, p. 42, Jun. 2019, doi: 10.1186/s40645-019-0282-1.
[18] P. Mensinga, J. Straube, and C. Schumacher, “Assessing the Freeze-Thaw Resistance of Clay Brick for Interior Insulation Retrofit Projects,” p. 11.
[19] P. Mensinga, “Determining the Critical Degree of Saturation of Brick Using Frost Dilatometry,” Aug. 2009, Accessed: Jun. 01, 2022. [Online]. Available: https://uwspace.uwaterloo.ca/handle/10012/4638
[20] J. Kočí, J. Maděra, M. Keppert, and R. Černý, “Damage functions for the cold regions and their applications in hygrothermal simulations of different types of building structures,” Cold Reg. Sci. Technol., vol. 135, pp. 1–7, Mar. 2017, doi: 10.1016/j.coldregions.2016.12.004.
[21] X. Zhou, D. Derome, and J. Carmeliet, “Hygrothermal modeling and evaluation of freeze-thaw damage risk of masonry walls retrofitted with internal insulation,” Build. Environ., vol. 125, pp. 285–298, Nov. 2017, doi: 10.1016/j.buildenv.2017.08.001.
[22] E. Vereecken, L. Van Gelder, H. Janssen, and S. Roels, “Interior insulation for wall retrofitting – A probabilistic analysis of energy savings and hygrothermal risks,” Energy Build., vol. 89, pp. 231–244, Feb. 2015, doi: 10.1016/j.enbuild.2014.12.031.
[23] X. Zhou, D. Derome, A. Kubilay, and J. Carmeliet, “Comprehensive Study of Moisture Risk on Building Facades Based on Spatial Distribution of Wetting and Drying,” 2022.
[24] J. Straube and E. F. P. Burnett, “Simplified prediction of driving rain on buildings, international building physics conference,” Eindh. Neth., pp. 375–382, Jan. 2000.
[25] S. Charisi, T. K. Thiis, P. Stefansson, and I. Burud, “Prediction model of microclimatic surface conditions on building façades,” Build. Environ., vol. 128, pp. 46–54, Jan. 2018, doi: 10.1016/j.buildenv.2017.11.017.
[26] S. Tsoka and T. K. Thiis, “Calculation of the driving rain wall factor using ray tracing,” J. Wind Eng. Ind. Aerodyn., vol. 179, pp. 190–199, Aug. 2018, doi: 10.1016/j.jweia.2018.06.008.
[27] T. K. Thiis, I. Burud, A. Flø, D. Kraniotis, S. Charisi, and P. Stefansson, “Monitoring and Simulation of Diurnal Surface Conditions of a Wooden Façade,” Procedia Environ. Sci., vol. 38, pp. 331–339, Jan. 2017, doi: 10.1016/j.proenv.2017.03.088.
[28] B. Blocken and J. Carmeliet, “Validation of CFD simulations of wind-driven rain on a low-rise building facade,” Build. Environ., vol. 42, no. 7, pp. 2530–2548, Jul. 2007, doi: 10.1016/j.buildenv.2006.07.032.
[29] A. Kubilay, D. Derome, B. Blocken, and J. Carmeliet, “Numerical simulations of wind-driven rain on an array of low-rise cubic buildings and validation by field measurements,” Build. Environ., vol. 81, pp. 283–295, Nov. 2014, doi: 10.1016/j.buildenv.2014.07.008.
[30] A. Khalilzadeh, H. Ge, and H. D. Ng, “Effect of turbulence modeling schemes on wind-driven rain deposition on a mid-rise building: CFD modeling and validation,” J. Wind Eng. Ind. Aerodyn., vol. 184, pp. 362–377, Jan. 2019, doi: 10.1016/j.jweia.2018.11.012.
[31] A. Kubilay, D. Derome, B. Blocken, and J. Carmeliet, “Wind-driven rain on two parallel wide buildings: Field measurements and CFD simulations,” J. Wind Eng. Ind. Aerodyn., vol. 146, pp. 11–28, Nov. 2015, doi: 10.1016/j.jweia.2015.07.006.
[32] X. Zhou, A. Kubilay, D. Derome, and J. Carmeliet, “Comparison of wind-driven rain load on building facades in the urban environment and open field: A case study on two buildings in Zurich, Switzerland,” Build. Environ., vol. 233, p. 110038, Apr. 2023, doi: 10.1016/j.buildenv.2023.110038.
[33] A. Kubilay, D. Derome, and J. Carmeliet, “Coupling of physical phenomena in urban microclimate: A model integrating air flow, wind-driven rain, radiation and transport in building materials,” Urban Clim., vol. 24, pp. 398–418, Jun. 2018, doi: 10.1016/j.uclim.2017.04.012.
[34] “Computer-Aided Approach for Rapid Post-Event Visual Evaluation of a Building Façade.” Accessed: Oct. 01, 2024. [Online]. Available: https://www.mdpi.com/1424-8220/18/9/3017

[35] S. Sankarasrinivasan, E. Balasubramanian, K. Karthik, U. Chandrasekar, and R. Gupta, "Health Monitoring of Civil Structures with Integrated UAV and Image Processing System," Procedia Comput. Sci., vol. 54, pp. 508–515, Jan. 2015, doi: 10.1016/j.procs.2015.06.058.
[36] C. Eschmann, C. Kuo, C. Kuo, and C. Boller, "Unmanned Aircraft Systems for Remote Building Inspection and Monitoring," 2012. Accessed: Oct. 01, 2024. [Online]. Available: https://www.semanticscholar.org/paper/Unmanned-Aircraft-Systems-for-Remote-Building-and-Eschmann-Kuo/25af5ace3b8e925045a0f13587340c1fcbf14dcd
[37] F. C. Pereira and C. E. Pereira, "Embedded Image Processing Systems for Automatic Recognition of Cracks using UAVs," IFAC-Pap., vol. 48, no. 10, pp. 16–21, Jan. 2015, doi: 10.1016/j.ifacol.2015.08.101.
[38] C.-Z. Dong and F. N. Catbas, "A review of computer vision–based structural health monitoring at local and global levels," Struct. Health Monit., vol. 20, no. 2, pp. 692–743, Mar. 2021, doi: 10.1177/1475921720935585.
[39] K. Chen, G. Reichard, X. Xu, and A. Akanmu, "Automated crack segmentation in close-range building façade inspection images using deep learning techniques," J. Build. Eng., vol. 43, p. 102913, Nov. 2021, doi: 10.1016/j.jobe.2021.102913.
[40] Y. Chen, Z. Zhu, Z. Lin, and Y. Zhou, "Building Surface Crack Detection Using Deep Learning Technology," Buildings, vol. 13, no. 7, Art. no. 7, Jul. 2023, doi: 10.3390/buildings13071814.
[41] S. Katsigiannis, S. Seyedzadeh, A. Agapiou, and N. Ramzan, "Deep learning for crack detection on masonry façades using limited data and transfer learning," J. Build. Eng., vol. 76, p. 107105, Oct. 2023, doi: 10.1016/j.jobe.2023.107105.
[42] N. Wang, X. Zhao, P. Zhao, Y. Zhang, Z. Zou, and J. Ou, "Automatic damage detection of historic masonry buildings based on mobile deep learning," Autom. Constr., vol. 103, pp. 53–66, 2019, doi: 10.1016/j.autcon.2019.03.003.
[43] J. Guo, Q. Wang, Y. Li, and P. Liu, "Façade defects classification from imbalanced dataset using meta learning-based convolutional neural network," Comput.-Aided Civ. Infrastruct. Eng., vol. 35, no. 12, pp. 1403–1418, 2020, doi: 10.1111/mice.12578.
[44] "StainView: A Fast and Reliable Method for Mapping Stains in Facades Using Image Classification in HSV and CIELab Colour Space." Accessed: Oct. 01, 2024. [Online]. Available: https://www.mdpi.com/2072-4292/15/11/2895
[45] T. Rakha, A. Liberty, A. Gorodetsky, B. Kakillioglu, and S. Velipasalar, "Heat Mapping Drones: An Autonomous Computer-Vision-Based Procedure for Building Envelope Inspection Using Unmanned Aerial Systems (UAS)," Technol. Des., vol. 2, pp. 30–44, Jan. 2018, doi: 10.1080/24751448.2018.1420963.
[46] "Robust Pixel-Level Crack Detection Using Deep Fully Convolutional Neural Networks." Accessed: Oct. 01, 2024. [Online]. Available: https://ascelibrary.org/doi/epdf/10.1061/(ASCE)CP.1943-5487.0000854?src=getftr
[47] P. L. Gaspar and J. de Brito, "Quantifying environmental effects on cement-rendered facades: A comparison between different degradation indicators," Build. Environ., vol. 43, no. 11, pp. 1818–1828, Nov. 2008, doi: 10.1016/j.buildenv.2007.10.022.
[48] B. Lim, S. Son, H. Kim, S. Nah, and K. M. Lee, "Enhanced Deep Residual Networks for Single Image Super-Resolution," in 2017 IEEE Conference on Computer Vision and Pattern Recognition Workshops (CVPRW), Jul. 2017, pp. 1132–1140. doi: 10.1109/CVPRW.2017.151.
[49] Z. Niu and H. Li, "Research and analysis of threshold segmentation algorithms in image processing," J. Phys. Conf. Ser., vol. 1237, no. 2, p. 022122, Jun. 2019, doi: 10.1088/1742-6596/1237/2/022122.
[50] S. M.AqilBurney and H. Tariq, "K-Means Cluster Analysis for Image Segmentation," Int. J. Comput. Appl., vol. 96, no. 4, pp. 1–8, Jun. 2014, doi: 10.5120/16779-6360.
[51] J. Canny, "A Computational Approach to Edge Detection," in Readings in Computer Vision, M. A. Fischler and O. Firschein, Eds., San Francisco (CA): Morgan Kaufmann, 1987, pp. 184–203. doi: 10.1016/B978-0-08-051581-6.50024-6.

[52] A. Plaksyvyi, M. Skublewska-Paszkowska, and P. Powroznik, “A Comparative Analysis of Image Segmentation Using Classical and Deep Learning Approach,” Adv. Sci. Technol. Res. J., vol. 17, no. 6, pp. 127–139, Dec. 2023, doi: 10.12913/22998624/172771.
[53] N. O’Mahony et al., “Deep Learning vs. Traditional Computer Vision,” in Advances in Computer Vision, vol. 943, K. Arai and S. Kapoor, Eds., in Advances in Intelligent Systems and Computing, vol. 943. , Cham: Springer International Publishing, 2020, pp. 128–144. doi: 10.1007/978-3-030-17795-9_10.
[54] C. Szegedy, V. Vanhoucke, S. Ioffe, J. Shlens, and Z. Wojna, “Rethinking the Inception Architecture for Computer Vision,” 2016 IEEE Conf. Comput. Vis. Pattern Recognit. CVPR, pp. 2818–2826, Jun. 2016, doi: 10.1109/CVPR.2016.308.
[55] K. He, X. Zhang, S. Ren, and J. Sun, “Deep Residual Learning for Image Recognition,” in 2016 IEEE Conference on Computer Vision and Pattern Recognition (CVPR), Jun. 2016, pp. 770–778. doi: 10.1109/CVPR.2016.90.
[56] J. Redmon, S. Divvala, R. Girshick, and A. Farhadi, “You Only Look Once: Unified, Real-Time Object Detection,” in 2016 IEEE Conference on Computer Vision and Pattern Recognition (CVPR), Jun. 2016, pp. 779–788. doi: 10.1109/CVPR.2016.91.
[57] M. Tan, R. Pang, and Q. V. Le, “EfficientDet: Scalable and Efficient Object Detection,” in 2020 IEEE/CVF Conference on Computer Vision and Pattern Recognition (CVPR), Jun. 2020, pp. 10778–10787. doi: 10.1109/CVPR42600.2020.01079.
[58] W. Liu et al., “SSD: Single Shot MultiBox Detector,” vol. 9905, 2016, pp. 21–37. doi: 10.1007/978-3-319-46448-0_2.
[59] O. Ronneberger, P. Fischer, and T. Brox, “U-Net: Convolutional Networks for Biomedical Image Segmentation,” in Medical Image Computing and Computer-Assisted Intervention – MICCAI 2015, N. Navab, J. Hornegger, W. M. Wells, and A. F. Frangi, Eds., Cham: Springer International Publishing, 2015, pp. 234–241. doi: 10.1007/978-3-319-24574-4_28.
[60] J. Long, E. Shelhamer, and T. Darrell, “Fully convolutional networks for semantic segmentation,” presented at the 2015 IEEE Conference on Computer Vision and Pattern Recognition (CVPR), IEEE Computer Society, Jun. 2015, pp. 3431–3440. doi: 10.1109/CVPR.2015.7298965.
[61] V. Badrinarayanan, A. Kendall, and R. Cipolla, “SegNet: A Deep Convolutional Encoder-Decoder Architecture for Image Segmentation.,” IEEE Trans. Pattern Anal. Mach. Intell., vol. 39, no. 12, Dec. 2017, doi: 10.1109/TPAMI.2016.2644615.
[62] S. Ren, K. He, R. Girshick, and J. Sun, “Faster R-CNN: towards real-time object detection with region proposal networks,” in Proceedings of the 28th International Conference on Neural Information Processing Systems - Volume 1, in NIPS’15. Cambridge, MA, USA: MIT Press, Dec. 2015, pp. 91–99.
[63] N. Wang, X. Zhao, P. Zhao, Y. Zhang, Z. Zou, and J. Ou, “Automatic damage detection of historic masonry buildings based on mobile deep learning,” Autom. Constr., vol. 103, pp. 53–66, 2019, doi: 10.1016/j.autcon.2019.03.003.
[64] V. Naserentin, A. Logg, and D. Wästberg, “DTCC Builder: A mesh generator for automatic, efficient, and robust mesh generation for large-scale city modeling and simulation,” J. Open Source Softw., vol. 8, no. 86, 2023, doi: 10.21105/joss.04928.
[65] J. Mandinec and P. Johansson, “Towards an automatized and objective assessment of data from visual inspections of building envelopes,” Acta Polytech. CTU Proc., vol. 38, pp. 57–64, Dec. 2022, doi: 10.14311/APP.2022.38.0057.
[66] “Ladybug Tools | About.” Accessed: Mar. 10, 2025. [Online]. Available: https://www.ladybug.tools/about.html
[67] “Index, Welcome to DL-Light, Extension study daylit ambiance within SketchUp.” Accessed: Mar. 10, 2025. [Online]. Available: https://deluminaelab.com/dl-light/en/
[68] “INDALUX software package for characterizing solar and daylight access in urban areas.” Accessed: Mar. 10, 2025. [Online]. Available: https://phybat.heia-fr.ch/idlx/

[69] “WUFI® 2D | WUFI (en).” Accessed: Jan. 19, 2023. [Online]. Available: https://wufi.de/en/software/wufi-2d/
[70] M. Guizzardi, D. Derome, R. Vonbank, and J. Carmeliet, “Hygrothermal behavior of a massive wall with interior insulation during wetting,” Build. Environ., vol. 89, pp. 59–71, Jul. 2015, doi: 10.1016/j.buildenv.2015.01.034.
[71] R. Bellman, “Dynamic Programming,” Science, vol. 153, no. 3731, pp. 34–37, Jul. 1966, doi: 10.1126/science.153.3731.34.
[72] K. Pearson, “LIII. On lines and planes of closest fit to systems of points in space,” Lond. Edinb. Dublin Philos. Mag. J. Sci., vol. 2, no. 11, pp. 559–572, Nov. 1901, doi: 10.1080/14786440109462720.
[73] U. Stańczyk and L. C. Jain, Eds., Feature Selection for Data and Pattern Recognition, vol. 584. in Studies in Computational Intelligence, vol. 584. Berlin, Heidelberg: Springer, 2015. doi: 10.1007/978-3-662-45620-0.